Nonreflecting Boundary Conditions for Time Dependent Wave Propagation*

M.J. Grote

Research Report No. 2000-04
April 2000

Seminar für Angewandte Mathematik
Eidgenössische Technische Hochschule
CH-8092 Zürich
Switzerland

---

*To appear in “Artificial Boundary Conditions, with Applications to Computational Fluid Dynamics”, Ed. L. Tourrette, Nova Science Publishers Inc., New York

Nonreflecting Boundary Conditions for Time Dependent Wave Propagation*

M.J. Grote

Seminar für Angewandte Mathematik
Eidgenössische Technische Hochschule
CH-8092 Zürich
Switzerland

Research Report No. 2000-04 April 2000

Malgré moi l'infini me tourmente
Alfred de Musset

Abstract

Time dependent problems in unbounded media arise in many applications such as acoustic or electromagnetic scattering. Numerical methods can handle complicated geometries, inhomogeneous media, and nonlinearities. However, they require an artificial boundary, which truncates the unbounded exterior domain. Therefore an absorbing boundary condition needs to be applied at the artificial boundary to minimize the amount of spurious reflection from it. First, the derivation of the exact nonreflecting boundary condition for the one-dimensional wave equation is briefly reviewed. Next, the two- and three-dimensional cases are discussed, and the trade-off between exactness and locality exemplified through a short discussion of local absorbing boundary conditions. Then, the derivation of the nonreflecting boundary condition for the time wave equation in three space dimensions (Grote and Keller, 1995) is reviewed. The derivation is outlined without all the technical details and proofs, but instead by emphasizing the underlying main ideas. It is also shown how to combine the nonreflecting boundary condition both with the finite difference and the finite element methods. Finally, the accuracy and convergence properties of various absorbing and nonreflecting boundary conditions are compared via two numerical experiments.

---

[*] To appear in "Artificial Boundary Conditions, with Applications to Computational Fluid Dynamics", Ed. L. Tourrette, Nova Science Publishers Inc., New York

1 Introduction

Unbounded domains are often encountered in scientific and engineering applications. Examples are radar and sonar technology, wireless communication, aeroacoustics, fluid dynamics, earthquake simulations, or even quantum chemistry. Typically the phenomenon of interest is local but embedded in a vast surrounding medium. Although the exterior region is not truly unbounded, the boundary effects are often negligible, so that one further simplifies the problem by replacing the vast exterior by an infinite medium. Clearly the numerical computation of the flow past an airfoil does not require the simulation of the entire atmosphere.

Mathematical models of natural phenomena usually consist of partial differential equations, whose derivation is based on physical conservation laws (conservation of energy, etc.). Many standard numerical methods, such as finite differences and finite elements, can approximately solve partial differential equations. In fact, they can even handle complicated geometries, inhomogeneous media, and nonlinearity. However, they typically require an artificial boundary, which truncates the unbounded exterior domain, to fit the infinite region on a finite computer. This immediately raises the purely mathematical question:

> Which boundary condition guarantees that the solution to the initial-boundary value problem inside the artificial boundary coincides with the solution of the original problem in the unbounded region ?

If we exhibit a boundary condition, such that the fictitious boundary appears perfectly transparent, we shall call it “exact”. Otherwise it will correspond to an *approximate boundary condition*[1] and generate some spurious reflection, which travels back and spoils the solution everywhere in the computational domain. The resulting error in the computer simulation then consists of two independent error components: the discretization error of the numerical method used in the interior and the spurious reflection generated at the fictitious boundary. Unless both error components are reduced systematically, the numerical solution will not converge to the solution of the original problem in the unbounded region. Instead, if one fails to reduce the error

---

[1] *“...also called radiating, absorbing, silent, transmitting, transparent, open, free-space, and one-way boundary conditions.”, Givoli, 1991*

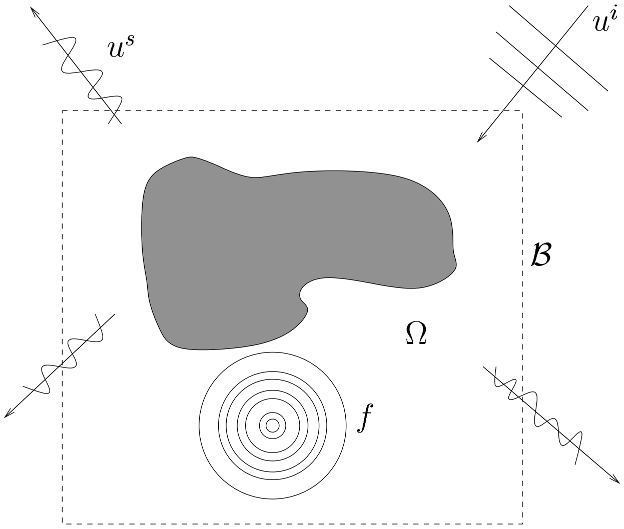

Figure 1: A typical scattering problem consists of an obstacle, a source term f, and incoming wave u^i, and a scattered wave u^s. The artificial boundary $\mathcal{B}$ defines the outer boundary of the computational domain Ω.

introduced at the artificial boundary while refining the underlying mesh, the numerical solution will converge to the solution of a different initial-boundary value problem with the approximate boundary condition.

1.1 Scattering Problems

In this article, we shall restrict ourselves to time dependent scattering problems. Typically a scattering problem consists of an obstacle, a source term f, and possibly an incident wave u^i – see Figure 1. Scattering problems are common in acoustic, electromagnetic, and elastic wave propagation. Our goal is to calculate numerically the time-dependent wave field u^s scattered from the complex, possibly nonlinear, but bounded scatterering region.

In 1974 Smith suggested perhaps the first exact method to restrict the computation to a finite region [2]. Let the computational domain Ω be bounded by a convex boundary of n line segments (or planar facets in $\mathbb{R}^3$). Then the restricition to Ω of the solution in unbounded space consists of a linear combination of 2^n solutions which satisfy all possible combinations of Dirichlet or Neumann boundary conditions. Unfortunately, this approach has but little practical value, since a rectangular domain requires $2^6 = 64$

independent numerical solutions. This example illustrates a key aspect in the design of improved absorbing boundary conditions: it is not sufficient to construct a new boundary condition; in addition, the computational effort involved must be comparable to that of the numerical method used in the interior. Otherwise it will quickly be dismissed as prohibitively expensive and impractical.

In Section 2, the derivation of the exact nonreflecting boundary condition for the one-dimensional wave equation is reviewed. Next, we consider the two- and three-dimensional cases in Section 3, and exemplify the trade-off between exactness and locality through a brief discussion of local absorbing boundary conditions. In Section 4, we shall review the derivation of the nonreflecting boundary condition of Grote and Keller [3] for the time dependent wave equation in three space dimensions. The derivation is outlined without technical details, but instead by emphasizing the main ideas. We shall then show how to combine the nonreflecting boundary condition both with the finite difference and the finite element method. Finally, we shall compare the accuracy and convergence properties of various absorbing and nonreflecting boundary conditions via two numerical experiments.

2 The One-dimensional Wave Equation

To illustrate the fundamental ideas underlying the derivation of absorbing boundary conditions, we begin with a simple one-dimensional problem. In this special situation many basic notions, in particular the exact boundary condition, appear in a very simple form. Nonetheless, we hasten to point out that its appealing simplicity is also misleading: the real challenges in deriving effective absorbing boundary conditions appear only in higher dimensions. Indeed a one-dimensional wave can only propagate in two directions, to the left or to the right. In two or more dimensions, however, waves propagate in infinitely many directions.

We now consider the one-dimensional wave equation on the positive real axis,

$$\frac{\partial^2 u}{\partial t^2} - \frac{\partial^2 u}{\partial x^2} = f, \qquad x > 0,\ t > 0. \tag{1}$$

At the left boundary, $x = 0$, we require that the solution satisfies

$$u(0,t) = 0, \qquad t > 0. \tag{2}$$

Thus, $u(x,t)$ describes the position of an infinitely (or just very) long vibrating string, attached at its left end; hence, $u = 0$ corresponds to the state at rest. The one-dimensional wave equation (1) describes the propagation of small perturbations induced by the applied forcing $f(x,t)$. Here we have normalized the propagation speed to one by rescaling time appropriately. The initial conditions of the vibrating string are defined by its position and velocity at $t = 0$:

$$u(x,0) = U_0(x), \quad \frac{\partial}{\partial t}u(x,0) = V_0(x), \qquad x > 0. \tag{3}$$

It can be shown that the initial-boundary value problem (1)–(3) is well-posed: it has a unique solution, which depends continously on U_0, V_0, and f.

We now make the following assumption, which defines the local character of the problem: let the forcing vanish outside a bounded region next to the left boundary, that is let $f(x,t) = 0$ for $x \geq L$ and for all time $t > 0$. Then the positive real line separates into two distinct regions: the *bounded* interval $\Omega = [0, L]$ and the interval $[L, \infty)$, unbounded yet where the forcing vanishes identically. Both regions meet at the artificial boundary $\{x = L\}$, which consists only of a single point. Furthermore, we assume that the string is at rest in the exterior at $t = 0$: $U_0(x) = 0$ and $V_0(x) = 0$ for $x \geq L$. We now wish to simulate numerically the time dependent behavior of the vibrating string in the computational domain Ω – by adding nonlinear effects it would be easy to complicate matters further and prevent any attempt to solve the problem analytically.

Unfortunately, we cannot apply our favorite numerical scheme in Ω and simply ignore the new artificial boundary point. On the contrary, we must pay close attention to the new boundary point at $x = L$: without a boundary condition at $x = L$, the initial value problem (1)–(3) restricted to Ω is not even well-posed. To derive a boundary condition, we first need to better understand its role at the artificial boundary. Suppose a wave propagates to the right inside Ω and reaches the right boundary at $x = L$. It must not be reflected, for any spurious reflection will travel back into the computational domain and spoil the solution everywhere. This spurious reflection, caused by an inaccurate treatment of the artificial boundary, is not due to finite precision, unlike discretization errors present in any computation. If we find a boundary condition, which lets the waves hit the boundary without any reflection, the solution inside Ω, with that boundary condition imposed at $x = L$, coincides with the restriction to Ω of the solution in the unbounded

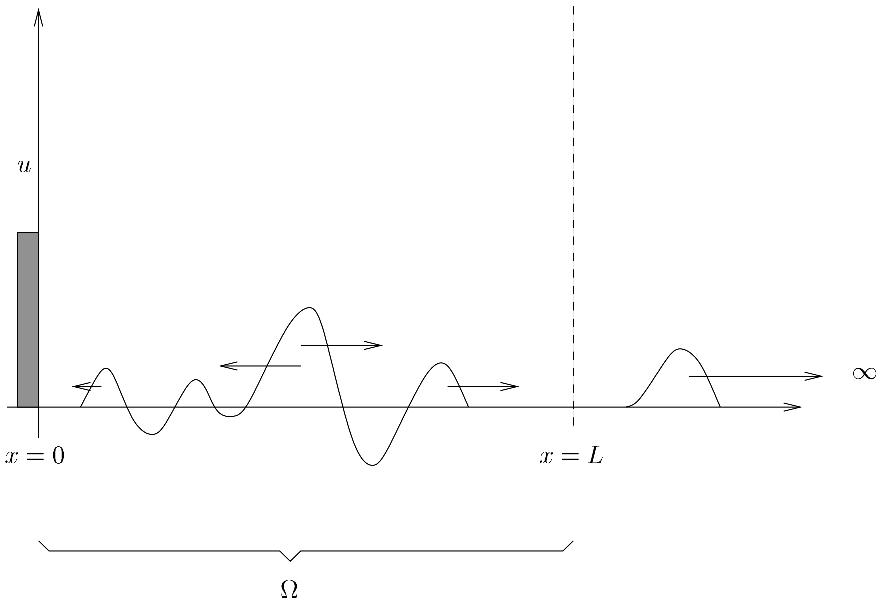

Figure 2: The one-dimensional wave equation: inside the computational domain, $\Omega = [0, L]$ the problem can be arbitrarily complicated, but in the exterior region, $x \geq L$, we assume that $f(x, t) = 0$ for $t > 0$ and that u and $\partial_t u$ vanish at $t = 0$.

region. Hence such a boundary condition is *exact*.

Inside the computational domain Ω waves propagate both to the left and to the right. In the exterior region, however, the absence of any forcing and the zero initial conditions preclude the appearance of any waves traveling to the left: there all waves propagate eastward towards infinity – see Figure 2. To derive the exact boundary condition at $x = L$ we first need to separate the incoming from the outgoing waves. To do so, we let v and w be defined by

$$v = \frac{\partial u}{\partial t} + \frac{\partial u}{\partial x}, \qquad w = \frac{\partial u}{\partial t} - \frac{\partial u}{\partial x}. \tag{4}$$

Since u satisfies the wave equation (1) in $x \geq L$, we conclude that

$$\frac{\partial v}{\partial t} - \frac{\partial v}{\partial x} = 0, \qquad \frac{\partial w}{\partial t} + \frac{\partial w}{\partial x} = 0.$$

Thus we can rewrite (1) as the first-order hyperbolic system:

$$\frac{\partial}{\partial t}\begin{bmatrix} v \\ w \end{bmatrix} + \begin{bmatrix} -1 & 0 \\ 0 & 1 \end{bmatrix} \frac{\partial}{\partial x}\begin{bmatrix} v \\ w \end{bmatrix} = 0. \tag{5}$$

Its general solution is

$$v(x, t) = \phi(x + t), \qquad \text{and} \qquad w(x, t) = \psi(x - t),$$

where ϕ and ψ are arbitrary functions, which are determined by initial and boundary conditions. Therefore, v is constant on the characteristics $x+t=c$, whereas w remains constant on the characteristics $x-t=c$. Thus v corresponds to incoming waves, whereas w corresponds to outgoing waves. Since there are no incoming waves in $x \geq L$, we have

$$v(L,t)=0, \qquad t>0. \tag{6}$$

By applying the definition (4) of v in (6) we thus obtain the exact nonreflecting boundary condition for the displacement $u(x,t)$,

$$\left(\frac{\partial}{\partial t}+\frac{\partial}{\partial x}\right)u=0, \qquad x=L, \quad t>0. \tag{7}$$

We shall now test the boundary condition (7) via a numerical experiment. We consider (1)–(3) with $f=0$ and $V_0=0$, and assume that U_0 vanishes outside $x \geq 1$. Next, we restrict the computational domain to the interval $0 \leq x \leq 1$ and impose the exact boundary condition (7) at $x=1$. Both (1) and (7) are discretized with second-order finite differences in space and time. In Figure 3 we observe the time dependent evolution of a small perturbation, initially located inside Ω. The initial perturbation immediately separates into two independent waves which propagate in opposite directions. While the first wave proceeds to the right and leaves the computational domain at $x=1$, the second wave propagating to the left encounters the 'wall' boundary at $x=0$, changes its sign and direction, and eventually follows the first wave only to vanish as well at $x=1$. Thanks to the exact boundary condition (7), the fictitious boundary at $x=1$ appears perfectly transparent to both waves as they leave Ω without any spurious reflection. Again we emphasize that the problem inside Ω can be arbitrarily complicated, since the derivation of the (exact) nonreflecting boundary condition (7) depends only on properties in the exterior region.

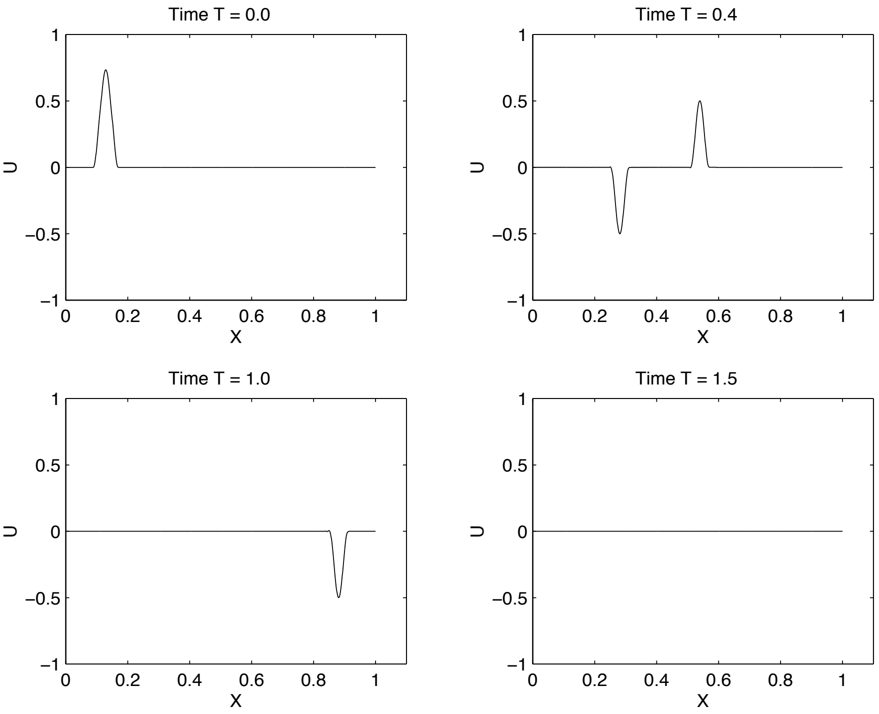

Figure 3: Numerical solution of the one-dimensional wave equation in a semi-infinite interval. The initial perturbation separates into two independent waves, which propagate in opposite directions (Not shown). Upon arrival at the left 'wall' boundary, the initially left moving wave is reflected back (It is shown at time $t = 0.4$.). It then follows the first right-moving wave up to the artificial boundary at $x = 1$, where both waves leave Ω without any spurious reflection.

3 Absorbing Boundary Conditions in Higher Dimensions

In this section we consider a highly complex but local scatterer located on the infinite two-dimensional plane. Although we shall restrict ourselves to the two-dimensional case, much of the present discussion carries over immediately to the three-dimensional case. To separate the local phenomenon of interest from the unbounded surrounding region, we first choose a closed curve, which circumscribes the scattering problem. Outside this curve, the (acoustic) medium is homogeneous, isotropic, and source free; thus all waves which cross this artificial boundary are purely outgoing. Although the shape and position of this curve are arbitrary, it should be convex to ensure that waves which have left the computational domain will never return. The most commonly used artificial boundary is rectangular, mainly because of the simple form of the wave equation in Cartesian coordinates.

We now consider the wave equation on the two-dimensional infinite plane,

$$\frac{\partial^2 u}{\partial t^2} - \frac{\partial^2 u}{\partial x^2} - \frac{\partial^2 u}{\partial y^2} = f, \qquad t > 0, \tag{8}$$

with the initial conditions

$$u(x, y, 0) = U_0(x, y), \quad \frac{\partial}{\partial t} u(x, y, 0) = U_1(x, y), \qquad t = 0.$$

By scaling time appropriately we have normalized the speed of propagation to one. Again the phenomenon of interest is very complicated, possibly nonlinear, but local. Next, we truncate the unbounded exterior by an artificial boundary and restrict the computation to the square $\Omega = [-L, L] \times [-L, L]$ – see Figure 1. Outside Ω we assume that neither source terms nor initial perturbations are present:

$$U_0(x, y) = U_1(x, y) = 0, \quad \text{and} \quad f(x, y, t) = 0, \; t > 0, \qquad (x, y) \in \mathbb{R}^2 \setminus \Omega.$$

Again we seek a boundary condition at $(x, y) \in \mathcal{B}$, which ensures that all waves reach the exterior region unharmed and without generating any unphysical reflection at the fictitious interface. Because of symmetry we only need to consider a single edge of the rectangle, here the right edge at $x = L$. Hence the exterior region lies to the right and the computational domain Ω to the left of the artificial boundary $\{(x, y) \in \mathbb{R}^2 | x = L\}$. Since the initial conditions and the forcing vanish identically in the exterior, all waves in the region $x \geq L$ are purely outgoing and must propagate eastward. To avoid any spurious reflection at $x = L$, the exact boundary condition must annihilate all incoming waves. In the previous section we easily derived such an exact nonreflecting boundary condition for the one-dimensional wave equation. Unfortunately, the same approach does not apply in two dimensions. In contrast to the one-dimensional case, any fixed location (L, y) at the artificial boundary receives incoming waves from not one but infinitely many angles of incidence, which propagate in infinitely many directions. The distinction between incoming and outgoing waves is now “infinitely more complicated”.

Let $\hat{u}(x,\xi,\omega)$ denote the Fourier transform of the solution $u(x,y,t)$ in time and in the tangential plane, parallel to the artificial boundary,

$$\hat{u}(x,\xi,\omega) = \int\limits_{-\infty}^{\infty}\int\limits_{-\infty}^{\infty} u(x,y,t)\, e^{i(\omega t+\xi y)}\, dy\, dt. \tag{9}$$

Here we have set the solution $u(x,y,t)$ to zero for all previous time $t < 0$. Then u is related to $\hat{u}$ via the inverse Fourier transform, which resembles (9) after exchanging u and $\hat{u}$. Since u satisfies the wave equation (8) with $f = 0$ for $x \geq L$, its Fourier transform satisfies

$$\frac{\partial^2}{\partial x^2}\hat{u} = (\xi^2 - \omega^2)\,\hat{u}, \qquad x \geq L. \tag{10}$$

To derive an exact nonreflecting boundary condition at $x = L$ we need to relate the normal derivative – here $\partial_x u$ – to tangential and time derivatives – here $\partial_y u$ and $\partial_t u$. From (10) we conclude that $\partial_x \hat{u}$ is determined by $\pm\sqrt{\xi^2 - \omega^2}\,\hat{u}$. The sign in front of the square root discriminates precisely incoming from outgoing waves; here the correct choice leads to the following exact boundary condition:

$$\frac{\partial}{\partial x}\hat{u} = -i\omega\,\sqrt{1-(\xi/\omega)^2}\,\hat{u}, \qquad x = L. \tag{11}$$

Although this boundary condition ensures the absoute transparency of the artificial boundary, this formulation has but little value in practice. Indeed, we do not seek a boundary condition for $\hat{u}$ but instead for u. In theory we can always compute the inverse transform and thus determine $\partial_x u$. However, unlike a polynomial expression, whose inverse Fourier transform yields a local differential operator, the inverse transform of the above expression does not result in a simple differential operator because of the square root. Instead, we obtain a so-called *pseudo-differential operator*, which cannot be evaluated without forward and inverse Fourier transform. As a consequence, the normal derivative $\partial_x u$ at any given point on the boundary (L, y) depends on past values of u on the entire line $x = L$, and cannot be computed locally either in space or time.

> *"...unfortunately, these [perfectly absorbing] boundary conditions have to be nonlocal in both space and time",* *Engquist & Majda, 1977*

3.1 Absorbing boundary conditions

To overcome the difficulties associated with the nonlocal nature of the exact boundary condition (11), we can replace the above pseudo-differential operator by an *approximate* differential operator. In doing so we give up on the absolute transparency of the artificial boundary and accept some spurious reflection. Such absorbing boundary conditions were proposed by Engquist and Majda [4] in 1977, and we now briefly recall the fundamental ideas underlying this popular approach.

The Fourier transform of a differential operator always results in a polynomial expression in the frequency domain. For instance the Fourier transform of the differential operator ∂_{yy} yields the polynomial $-\xi^2$. Conversely every polynomial in Fourier space corresponds to a (local) differential operator in physical space. Thus, the inverse Fourier transform of a polynomial in $s = \xi/\omega$, which approximates $\sqrt{1-s^2}$, will yield a differential operator, which can be used as an (approximate) absorbing boundary condition in physical space.

For s sufficiently small, we approximate $\sqrt{1-s^2}$ by the first few terms of its Taylor expansion:

$$\sqrt{1-s^2} = 1 - \frac{s^2}{2} + O(s^4), \qquad |s| \to 0.$$

We now replace the square root in (11) by the leading term in the Taylor expansion, that is $\sqrt{1-s^2} \simeq 1$, and perform the inverse Fourier transform to obtain

$$\begin{aligned} \frac{\partial \hat{u}}{\partial x} &\simeq -i\omega\,\hat{u} \\ &\Rightarrow \left(\frac{\partial}{\partial t} + \frac{\partial}{\partial x}\right) u = 0, \qquad x = L. \end{aligned}$$

This is the first-order Engquist-Majda boundary condition, which contains only first derivatives of the solution. It coincides with the exact boundary condition (7) for the one-dimensional wave equation. Therefore, it remains exact for solutions of the two-dimensional wave equation, which depend only on x and t and thus impinge on the artificial boundary with a normal angle of incidence. Next, we include one additional term of the Taylor expansion in the approximation, $\sqrt{1-s^2} \simeq 1 - s^2/2$. This yields the second-order

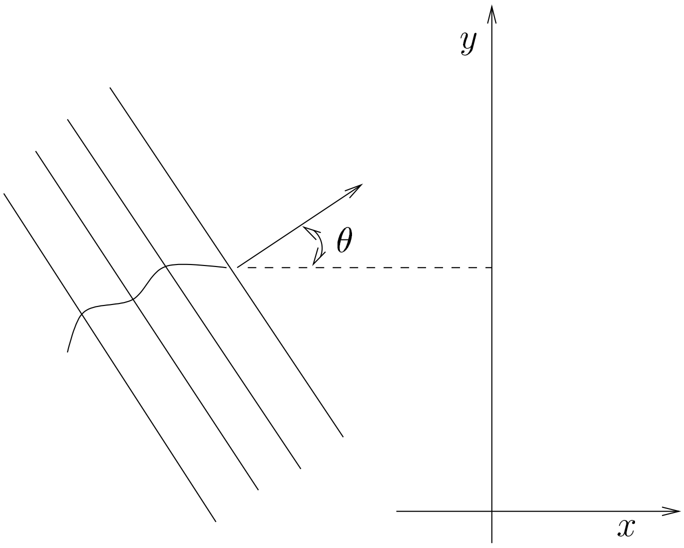

Figure 4: A traveling plane wave with an angle of incidence θ.

Engquist-Majda boundary condition,

$$\begin{aligned}\frac{\partial \hat{u}}{\partial x} &\simeq -i\omega(1-(\xi/\omega)^2/2)\,\hat{u}\\ &\Rightarrow \left(\frac{\partial^2}{\partial t^2}+\frac{\partial^2}{\partial x\,\partial t}-\frac{1}{2}\frac{\partial^2}{\partial y^2}\right)u=0, \qquad x=L. \qquad (12)\end{aligned}$$

Equation (12) remains exact at normal incidence, since we can rewrite it in the equivalent form as

$$(\partial_t+\partial_x)\,(\partial_t+\partial_x)\;u=0, \qquad x=L, \qquad (13)$$

by using (8). The inclusion of even higher order terms of the Taylor expansion to improve the accuracy of the approximation ceases to yield well-posed boundary conditions. Although this difficulty can be overcome by the use of rational (Padé) approximations, the high-order derivatives involved in these boundary conditions greatly complicate their use in any numerical scheme. As a result, first- and second-order boundary conditions are most commonly used in practice.

Various other (e.g. Chebychev) approximations of $\sqrt{1-s^2}$ were proposed to design improved local boundary conditions. Eventually, Higdon [5] showed that all these boundary conditions are particular cases of the following general class of boundary operators, where $\alpha_1, \ldots, \alpha_p$ are arbitrary parameters:

$$\left(\cos\alpha_p \frac{\partial}{\partial t} + \frac{\partial}{\partial x}\right) \ldots \left(\cos\alpha_1 \frac{\partial}{\partial t} + \frac{\partial}{\partial x}\right) u = 0, \qquad x = L. \tag{14}$$

For instance, the second-order Engquist-Majda boundary condition (13) results from setting $\alpha_1 = 0^\circ$ and $\alpha_2 = 0^\circ$ in (14). This general formulation, written as the product of first-order differential operators $(\cos\alpha_i\, \partial_t + \partial_x)$, provides a new, more intuitive, interpretation for the effectiveness of absorbing boundary conditions. Since any such differential operator perfectly annihilates plane waves with angle of incidence $\pm\alpha_i$, the artificial boundary will appear absolutely transparent at the discrete angles of incidence $\alpha_1, \ldots, \alpha_p$. The choice of $\alpha_1, \ldots, \alpha_p$ is arbitrary and can be adapted to any given situation.

Nevertheless, all absorbing boundary conditions remain only approximations to the exact boundary condition (11); therefore, they generate some spurious reflection at $x = L$. How large is the amount of reflection for a specific boundary condition ? Recall that any solution of the (homogeneous) wave equation can be represented by the superposition of plane waves. In Figure 4 we observe a plane wave, which impinges on the artificial boundary at $x = L$ with an angle of incidence θ. The linearity of both the wave equation (8) and the boundary condition (14) imply that any reflected wave necessarily propagates with the same frequency as the incident wave. Hence the solution consists of an outgoing wave, whose amplitude we normalize to one, and an incoming spurious wave with amplitude $|r|$:

$$u(x, y, t) = e^{i(kx + \ell y - \omega t)} + r e^{i(-kx + \ell y - \omega t)}, \qquad k, \omega \geq 0, \tag{15}$$

Here $r = r(\theta; \alpha_1, \ldots, \alpha_p)$ depends on the angle of incidence θ, defined by $\tan\theta = \ell/k$, and the fixed parameters $\alpha_1, \ldots, \alpha_p$. In Figure 5 we compare the effectiveness of three absorbing boundary conditions by displaying the amount of reflection $|r|$ versus the angle of incidence θ. The choice $\alpha_1 = 0^\circ$ corresponds to the first, whereas $\alpha_1 = 0^\circ$ und $\alpha_2 = 0^\circ$ corresponds to the second Engquist-Majda boundary condition. Alternatively, the popular parameter choice $\alpha_1 = 0^\circ$ and $\alpha_2 = 60^\circ$ annihilates incoming waves at normal incidence and at 60° angle of incidence. All other angles of incidence will generate some spurious reflection, which is very small close to normal incidence but rapidly increases as grazing incidence is approached.

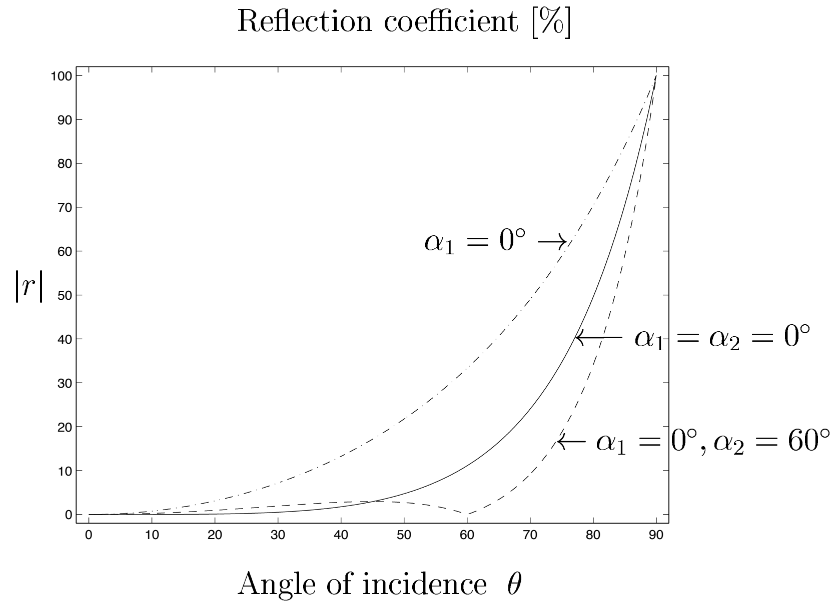

Figure 5: Amount of spurious reflection (in percent) caused by the use of the boundary conditions (14) for a plane wave with angle of incidence θ.

4 Exact nonreflecting boundary conditions

Instead of using an approximate local boundary condition, Ting and Miksis [6] proposed in 1986 to represent the exact solution in the exterior region by using Kirchhoff's formula; this approach was later implemented by Givoli and Cohen [7]. Kirchhoff's integral representation translates Huygens' purely geometric principle to an analytic formulation: the scattered wave field in the exterior is a superposition of infinitely many spherical waves, generated by a continuous source distribution on the artificial boundary $\mathcal{B}$. As a consequence, the solution at any point on $\mathcal{B}$ is determined by past values of the solution on some intermediate surface $\mathcal{S}$ inside Ω. Let N be the number of grid points in one dimension. Then, a standard time-marching scheme typically requires about N^3 operations per time step. In contrast, the evaluation of the retarded potentials necessary to update the solution at $\mathcal{B}$ require N^4 operations per time step. Therefore, advancing the solution at $\mathcal{B}$ is usually more expensive than applying the numerical scheme itself inside Ω. Moreover, Kirchhoff's integral representation of the solution requires storing the past values of the solution on $\mathcal{S}$ for the length of time it takes a wave to propagate across the computational domain.

Neither local absorbing boundary conditions nor exact boundary conditions based on Kirchhoff's integral formula fully satisfy the demand for increasingly accurate and efficient numerical methods to solve complex time-dependent scattering problems in unbounded domains. On the one hand, local absorbing boundary conditions are simple to use but generate spurious reflection at the artificial boundary, and on the other hand, boundary conditions based on the space-time integral representation are exact but prohibitively expensive, because of their computational cost and memory requirements.

In the special case when $\mathcal{B}$ is a sphere, however, it is possible to derive an exact nonreflecting boundary condition which is global over the artificial boundary but *local in time* [3, 8] – another form of this exact boundary condition was obtained by Sofronov [9, 10]. This new formulation avoids any integrals over the past of the solution, and thus requires little extra computational effort and memory. It was later generalized to electromagnetic waves [11], and more recently to elastic waves [12, 13]. We shall now present the main ideas underlying the derivation in [3].

4.1 Derivation of the boundary condition

We consider time dependent scattering from a bounded scattering region in three-dimensional space. Next, we surround this region by a sphere $\mathcal{B}$ of radius R. Outside $\mathcal{B}$, we assume that the scattered field $u(\boldsymbol{x}, t)$ satisfies the homogeneous wave equation with constant propagation speed $c > 0$,

$$\frac{\partial^2 u}{\partial t^2} - c^2 \Delta u = 0. \tag{16}$$

Furthermore, we assume that the initial conditions vanish outside $\mathcal{B}$,

$$u(\boldsymbol{x}, 0) = 0, \qquad \partial_t u(\boldsymbol{x}, 0) = 0, \qquad |\boldsymbol{x}| \geq R. \tag{17}$$

Although identically zero initially, the solution u does not remain zero with increasing time, as the waves generated inside $\mathcal{B}$ radiate into the exterior unbounded region.

To solve (16) outside $\mathcal{B}$, we first introduce the polar coordinates r, θ, φ and the nm-th spherical harmonic $Y_{nm}(\theta, \varphi)$, normalized over the *unit* sphere,

$$Y_{nm}(\theta, \varphi) = \sqrt{\frac{(2n+1)(n-|m|)!}{4\pi(n+|m|)!}} P_n^{|m|}(\cos\theta)\, e^{im\varphi}, \tag{18}$$

where $P_n^{|m|}$ is the Legendre function. Here the ϑ coordinate corresponds to the angle from the z-axis, $\vartheta \in [0,\pi]$, whereas the ϕ coordinate corresponds to the polar angle in the (x,y)-plane, $\phi \in [0,2\pi)$. If the problem considered is real, it is advantageous to use the spherical harmonics, given by the real and imaginary parts of (18). Then everything remains the same except for the normalization constant in (18), which must be multiplied by $\sqrt{2}$ for $m \neq 0$.

Outside $\mathcal{B}$ the solution admits the Fourier series representation

$$u(\boldsymbol{x},t) = \sum_{n=0}^{\infty} \sum_{m=-n}^{n} u_{nm}(r,t) Y_{nm}(\theta,\varphi). \tag{19}$$

Hence $u_{nm}(r,t)$ is given by

$$u_{nm}(r,t) = \int_0^{2\pi} \int_0^{\pi} u(r,\theta,\varphi,t) \overline{Y_{nm}}(\theta,\varphi) sin\theta \, d\theta \, d\varphi. \tag{20}$$

It follows from (16)–(17) that u_{nm}, with $|m| \leq n$, satisfies

$$\left(\frac{1}{c^2} \frac{\partial^2}{\partial t^2} - \frac{\partial^2}{\partial r^2} - \frac{2}{r} \frac{\partial}{\partial r} + \frac{n(n+1)}{r^2} \right) u_{nm} = 0, \qquad r \geq R, \quad t > 0, \tag{21}$$

with the initial conditions

$$u_{nm}(r,0) = 0, \qquad \partial_t u_{nm}(r,0) = 0, \qquad r \geq R. \tag{22}$$

We have now replaced (16)–(17) by the problem of solving (21)–(22) for each m and n. Our goal is to find a boundary condition at $r = R$ for each (m,n), so that the solution in $0 \leq r \leq R$ with this condition concides with the restriction to $0 \leq r \leq R$ of u_{nm} for all $t \geq 0$.

THE CASE $n = 0$:

For $n = 0$, Y_{00} is constant and the solution $u = u_{00}(r,t) Y_{00}$ is independent of ϑ, ϕ. Thus, u corresponds to a spherically symmetric outgoing wave; moreover, ru satisfies the one-dimensional wave equation,

$$\frac{\partial^2}{\partial t^2}(ru) - c^2 \frac{\partial^2}{\partial r^2}(ru) = 0, \qquad r \geq R.$$

As both u and $\partial_t u$ vanish outside $\mathcal{B}$ at $t = 0$, we conclude (see Section 2) that the exact nonreflecting boundary condition for $u(r,t)$ is

$$\left(\frac{\partial}{\partial r} + \frac{1}{c} \frac{\partial}{\partial t} \right) [ru] = 0, \qquad r = R,$$

or equivalently

$$\frac{\partial u}{\partial r} + \frac{1}{c}\frac{\partial u}{\partial t} + \frac{u}{R} = 0, \qquad r = R.$$

For three-dimensional waves this boundary condition is exact at normal incidence only.

THE CASE $n = 1$:

We now wish to derive an exact boundary condition for $u_{1m}(r,t)$, which satisifies (21) with $n = 1$:

$$\left(\frac{1}{c^2}\frac{\partial^2}{\partial t^2} - \frac{\partial^2}{\partial r^2} - \frac{2}{r}\frac{\partial}{\partial r} + \frac{2}{r^2}\right) u_{1m} = 0, \qquad r \geq R. \tag{23}$$

First, we shall transform u_{1m} to a new variable v, which satisfies the one-dimensional wave equation. To do so, we recall that if $v = v(r,t)$ satisfies

$$\frac{\partial^2 v}{\partial t^2} - c^2 \frac{\partial^2 v}{\partial r^2} = 0, \tag{24}$$

then

$$u = \frac{\partial}{\partial r}\frac{v}{r}$$

satisfies (23). Next, we drop the indices on $u = u_{1m}(r,t)$, and invert the result above. Let

$$v(r,t) = r \int_r^\infty u(s,t)\, ds. \tag{25}$$

Then v satisfies (24), and both v and $\partial_t v$ vanish outside $\mathcal{B}$ at $t = 0$. Therefore, the exact boundary condition for v is

$$\left(\frac{\partial}{\partial r} + \frac{1}{c}\frac{\partial}{\partial t}\right) v(r,t) = 0, \qquad r = R. \tag{26}$$

We remark that the integral in (25) is finite for every t, because $u(r,t)$ vanishes for $r \geq R + c\,t$.

To use (26) in computation, we shall reformulate it and derive an equivalent but more tractable form, which does not involve integrals or high-order derivatives. To do so, we first calculate

$$\frac{\partial v}{\partial r} = \int_r^\infty u(s,t)\, ds - ru = \frac{v}{r} - ru. \tag{27}$$

We now use (26) to obtain

$$\frac{1}{c}\frac{\partial v}{\partial t} = -\frac{\partial v}{\partial r} = -\frac{v}{r} + ru. \tag{28}$$

Next, we apply $\partial_r + c^{-1}\partial_t$ to (28) and again use (26), which leads to

$$\left(\frac{\partial}{\partial r} + \frac{1}{c}\frac{\partial}{\partial t}\right) ru(r,t) = \left(\frac{\partial}{\partial r} + \frac{1}{c}\frac{\partial}{\partial t}\right)\left[\frac{1}{c}\frac{\partial}{\partial t}v + \frac{v}{r}\right] = -\frac{v}{r^2}. \tag{29}$$

We now set $r = R$ and let $\psi(t) = v(R,t)/R$ in (29) to obtain

$$\left(\frac{\partial}{\partial r} + \frac{1}{c}\frac{\partial}{\partial t}\right) ru = -\frac{\psi(t)}{R}, \qquad r = R. \tag{30}$$

Equation (30) in an exact boundary condition for u, but it still involves the a priori unknown quantity $\psi(t)$. To determine it we set $r = R$ in (28), which after division by R yields the *ordinary differential equation*

$$\frac{1}{c}\frac{d\psi(t)}{dt} = -\frac{\psi(t)}{R} + u(R,t), \qquad \psi(0) = 0. \tag{31}$$

We note that $\psi(0) = 0$ because $v(r,t)$ vanishes for $r \geq R$ at $t = 0$.

THE GENERAL CASE $n \geq 0$:

The procedure presented in the two previous sections for $n = 0$ and $n = 1$ can be extended to the general case for all n. We refrain from repeating here in detail this derivation [3] and restrict ourselves to a summary of the main steps involved.

First, we let G_n be the integral operator

$$G_n[u](r,t) \equiv \begin{cases} ru(r,t) & \text{if } n = 0 \\ \\ r\displaystyle\int_r^\infty \frac{(r^2 - s^2)^{n-1}u(s,t)}{(2s)^{n-1}(n-1)!}\,ds & \text{if } n \geq 1. \end{cases} \tag{32}$$

Since the initial data has compact support and since the speed of propagation is finite, at any fixed time $u_{nm}(r,t)$ vanishes for r sufficiently large. Therefore, the integral in (32) with u replaced by u_{nm} exists for each n.

Next, we apply G_n to $u_{nm}(r,t)$, and find (see [3] for details) that $G_n[u_{nm}]$ satisfies the one-dimensional wave equation outside $\mathcal{B}$:

$$\frac{\partial^2}{\partial t^2}G_n[u_{nm}] - c^2\frac{\partial^2}{\partial r^2}G_n[u_{nm}] = 0, \qquad r \geq R.$$

Moreover, since both $G_n[u_{nm}]$ and $\partial_t G_n[u_{nm}]$ vanish outside $\mathcal{B}$ at $t = 0$, we conclude that

$$\left(\frac{\partial}{\partial r} + \frac{1}{c}\frac{\partial}{\partial t}\right) G_n[u_{nm}] = 0, \qquad r = R. \tag{33}$$

As $G_n[u_{nm}](r,t)$ is not known, (33) cannot be used directly in a numerical scheme. Therefore we shall reformulate the exact boundary condition (33) in terms of u_{nm} and other known quantities.

In [3] it was shown that

$$r u_{nm}(r,t) = \sum_{j=0}^{n} \frac{\gamma_{nj}}{r^j} \left(-\frac{\partial}{\partial r}\right)^{n-j} G_n[u_{nm}](r,t), \tag{34}$$

where the constants γ_{nj} are defined by

$$\gamma_{nj} = \frac{(n+j)!}{(n-j)!\, j!\, 2^j}. \tag{35}$$

We now apply $\partial_r + c^{-1}\,\partial_t$ to (34), set $r = R$, and use (33) to obtain

$$\left(\frac{\partial}{\partial r} + \frac{1}{c}\frac{\partial}{\partial t}\right) [r u_{nm}(r,t)]_{r=R} = -\frac{1}{R} \sum_{j=1}^{n} \frac{j\,\gamma_{nj}}{R^j\, c^{n-j}} \frac{\partial^{n-j}}{\partial t^{n-j}} G_n[u_{nm}](R,t). \tag{36}$$

Equation (36) is an exact nonreflecting boundary condition for u_{nm} on $\mathcal{B}$, but it involves time derivatives of $G_n[u_{nm}]$ up to order $n-1$. We note that a crucial consequence of applying $\partial_r + c^{-1}\partial_t$ to (34) is the elimination of the n-th derivative of $G_n[u_{nm}]$, the term with $j = 0$ in (34). To compute the time derivatives of $G_n[u_{nm}]$ up to order $n-1$ at $r = R$, we set $r = R$ in (34) and again use (33). The result is

$$\frac{1}{c^n}\frac{\partial^n}{\partial t^n} G_n[u_{nm}](R,t) = -\sum_{j=1}^{n} \frac{\gamma_{nj}}{R^j\, c^{n-j}} \left(\frac{\partial}{\partial t}\right)^{n-j} G_n[u_{nm}](R,t) + R\, u_{nm}(R,t). \tag{37}$$

Here we have used the fact that $\gamma_{n0} = 1$. Equation (37) is an n-th order ordinary differential equation for $G_n[u_{nm}](R,t)$.

To simplify the notation, we define the n-component vector function $\boldsymbol{\psi}_{nm}(t) = \{\psi_{nm}^j(t)\}$ by

$$\psi_{nm}^j(t) = \frac{\gamma_{nj}}{R^j\, \gamma_{n1} c^{n-j}} \left(\frac{\partial}{\partial t}\right)^{n-j} G_n[u_{nm}](R,t), \qquad j = 1, \ldots, n. \tag{38}$$

Here we have used an improved scaling in inverse powers of R, first suggested by Thompson and Huan [14]; this new scaling has no effect if $R = 1$. In addition, we let $\boldsymbol{d}_n = \{d_n^j\}$ denote the *constant* n-component vector

$$d_n^j = \gamma_{n1} j = \frac{n(n+1)j}{2}, \qquad j = 1, \ldots, n. \tag{39}$$

With these new variables (36) reduces to

$$\left(\frac{\partial}{\partial r} + \frac{1}{c}\frac{\partial}{\partial t}\right)(r u_{nm})\big|_{r=R} = -\frac{1}{R}\boldsymbol{d}_n \cdot \boldsymbol{\psi}_{nm}(t). \tag{40}$$

Next, we note that by definition of $\psi_{nm}^j(t)$ we have

$$\frac{1}{c}\frac{d}{dt}\psi_{nm}^j = \frac{\gamma_{nj}}{R\,\gamma_{n,j-1}}\,\psi_{nm}^{j-1} = \frac{(n+j)(n+1-j)}{2j\,R}\,\psi_{nm}^{j-1}, \qquad 2 \le j \le n. \tag{41}$$

Since u_{nm} and $\partial_t u_{nm}$ vanish identically for $r \ge R$ at $t = 0$, so do $G_n[u_{nm}]$ and all its time derivatives up to order $n-1$. This implies that $\boldsymbol{\psi}_{nm}$ is equal to zero at $t = 0$. Therefore, after dividing by R, we can rewrite (37) together with (41) as the *linear first-order ordinary* differential equation

$$\frac{1}{c}\frac{d}{dt}\boldsymbol{\psi}_{nm}(t) = \frac{1}{R}\boldsymbol{A}_n\boldsymbol{\psi}_{nm}(t) + u_{nm}(R,t)\,\boldsymbol{e}_n, \qquad \boldsymbol{\psi}_{nm}(0) = 0. \tag{42}$$

Here $\boldsymbol{e}_n = \{e_n^j\}$, $1 \le j \le n$, is the constant n-component unit vector

$$\boldsymbol{e}_n = [1, 0, \ldots, 0]^\top, \tag{43}$$

and $\boldsymbol{A}_n = \{A_n^{ij}\}$, $1 \le i, j \le n$, is the constant $n \times n$ matrix

$$A_n^{ij} = \begin{cases} -n(n+1)/2 & \text{if } i = 1, \\ (n+i)(n+1-i)/(2i) & \text{if } i = j+1, \\ 0 & \text{otherwise.} \end{cases} \tag{44}$$

We multiply the previous boundary condition by Y_{nm} and sum all modes over n and m. This yields the exact boundary condition at $r = R$ for $u = u(x, y, z, t)$:

$$\left(\frac{\partial}{\partial r} + \frac{1}{c}\frac{\partial}{\partial t}\right)[ru] = -\frac{1}{R}\sum_{n=1}^{\infty}\sum_{m=-n}^{n}\boldsymbol{d}_n \cdot \boldsymbol{\psi}_{nm} Y_{nm}, \qquad r = R, \tag{45}$$

$$\frac{1}{c}\frac{d}{dt}\boldsymbol{\psi}_{nm}(t) = \frac{1}{R}\boldsymbol{A}_n\boldsymbol{\psi}_{nm}(t) + \left(u|_{r=R}, Y_{nm}\right)\boldsymbol{e}_n, \quad \boldsymbol{\psi}_{nm}(0) = 0. \tag{46}$$

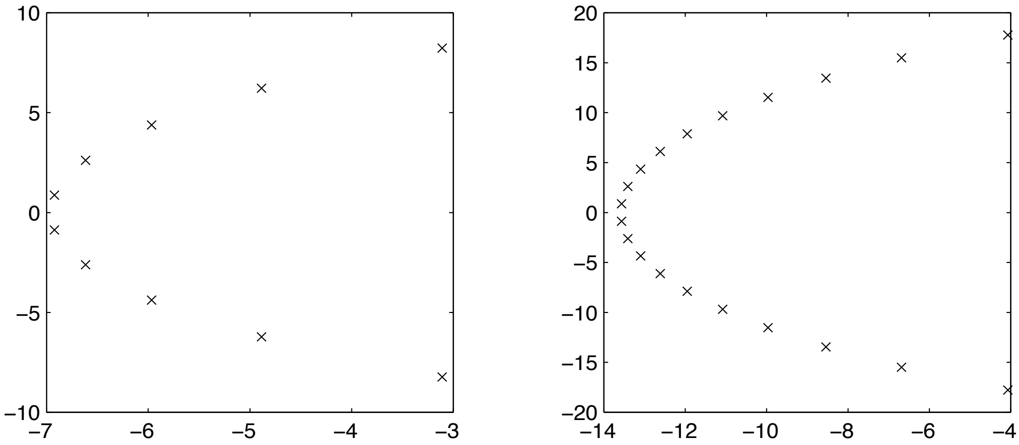

Figure 6: The eigenvalues of A_{10} (left) and A_{20} (right).

Here the constant vectors $\boldsymbol{e}_n$ and $\boldsymbol{d}_n$ are defined in (39) and (43), whereas the constant matrices $\boldsymbol{A}_n$ are defined in (44).

The exact nonreflecting boundary condition on u at $\mathcal{B}$ is given by (45). It involves only first derivatives of u together with the auxilliary functions $\boldsymbol{\psi}_{nm}(t)$. These functions can be computed by solving the linear first-order ordinary differential equations (46) concurrently with solving the problem for u in Ω. The boundary condition (45) is local in time, since past values of u are not required to apply it at time t. The necessary information from the past is contained implicitly in $\boldsymbol{\psi}_{nm}(t)$.

When used in computation, the boundary condition is approximated numerically. This introduces both discretization errors and rounding errors, which could trigger numerical instability. The stability of the ordinary differential equations (46), which are used to compute the auxilliary quantities $\boldsymbol{\psi}_{nm}(t)$, is determined by the eigenvalues of $\boldsymbol{A}_n$. In [8] we showed that the eigenvalues of $\boldsymbol{A}_n$ strictly lie in the left half of the complex plane and that the differential equation (46) is asymptotically stable. In fact, as n increases the maximal real part of the eigenvalues of $\boldsymbol{A}_n$ moves farther away from the imaginary axis, as shown in Figure 6. This results in a stronger obliteration of the past of $\boldsymbol{\psi}_{nm}(t)$ for higher Fourier modes on $\mathcal{B}$.

4.2 Finite Element Formulation

To show how to use the exact nonreflecting boundary condition (45) with the finite element method, we must derive the variational formulation of the problem considered. First, we need to specify a problem statement inside the computational domain Ω, with $|\boldsymbol{x}| \leq R$. For simplicity, we set $R = 1$ and normalize the speed of propagation outside Ω to one. In Ω, we consider the following simple model problem, together with the nonreflecting boundary condition (45) and (46), with $c = 1$ and $R = 1$:

$$
\begin{aligned}
\frac{\partial^2 u}{\partial t^2} - \nabla \cdot (c \nabla u) &= f \qquad \text{in } \Omega \times (0,T) && (47)\\
u(\boldsymbol{x},0) &= u_0(\boldsymbol{x}) \qquad \boldsymbol{x} \in \Omega && (48)\\
\frac{\partial}{\partial t} u(\boldsymbol{x},0) &= \dot{u}_0(\boldsymbol{x}) \qquad \boldsymbol{x} \in \Omega && (49)\\
\left(\frac{\partial}{\partial r} + \frac{\partial}{\partial t}\right)[ru] &= -\sum_{n=1}^{\infty} \sum_{m=-n}^{n} \boldsymbol{d}_n \cdot \boldsymbol{\psi}_{nm} Y_{nm} \qquad \text{on } \mathcal{B} \times (0,T) && (50)\\
\frac{d}{dt} \boldsymbol{\psi}_{nm}(t) &= \boldsymbol{A}_n \boldsymbol{\psi}_{nm}(t) + \left(u|_{r=1}, Y_{nm}\right) \boldsymbol{e}_n, \quad \boldsymbol{\psi}_{nm}(0) = 0. && (51)
\end{aligned}
$$

In (47) we require that $c = c(\boldsymbol{x}) > 0$. The source term $f(\boldsymbol{x}, t, u, \nabla u)$ may be nonlinear. The constant vectors $\boldsymbol{e}_n$ and $\boldsymbol{d}_n$ are defined in (39) and (43), whereas the constant matrices $\boldsymbol{A}_n$ are defined in (44).

We shall now derive the finite element formulation for the problem (47)–(51) in the computational domain Ω. To derive the weak form of the problem, we denote by $\mathcal{V}$ the Sobolev space $H^1(\Omega)$, which contains square-integrable functions with square-integrable first derivatives. Next we define the two inner products

$$
\begin{aligned}
(w,u) &= \int_\Omega \overline{w} u \, d\Omega, && (52)\\
(w,u)_{\mathcal{B}} &= \int_{\mathcal{B}} \overline{w} u \, d\mathcal{B}. && (53)
\end{aligned}
$$

We multiply (47)–(49) by a weighting function $\overline{w} \in \mathcal{V}$ and integrate over Ω. Then we use integration by parts in the integrated (47) to get

$$
(w, \ddot{u}) + (\nabla w, c \nabla u) - (w, \partial_r u)_{\mathcal{B}} = (w, f). \tag{54}
$$

Next, we use (50) to eliminate $\partial_r u$ on $\mathcal{B}$ from (54). These calculations lead to the weak form of the problem, which can be stated as follows:

Find $u(t) \in \mathcal{V}$ such that for all $w \in \mathcal{V}$,

$$\begin{aligned}
(w, \ddot{u}) \quad &+ \quad (\nabla w, c\nabla u) + (w, \dot{u} + u)_{\mathcal{B}} = (w, f) \\
&\quad -\sum_{n=1}^{\infty} \sum_{m=-n}^{n} \boldsymbol{d}_n \cdot \boldsymbol{\psi}_{nm} (w, Y_{nm})_{\mathcal{B}} && (55) \\
(w, u(0, .)) &= (w, u_0) && (56) \\
(w, \dot{u}(0, .)) &= (w, \dot{u}_0) && (57) \\
\dot{\boldsymbol{\psi}}_{nm}(t) &= \boldsymbol{A}_n \boldsymbol{\psi}_{nm}(t) + \left(u|_{r=1}, Y_{nm} \right) \boldsymbol{e}_n, \qquad \boldsymbol{\psi}_{nm}(0) = 0. && (58)
\end{aligned}$$

The finite element method [15] is obtained by approximating the weak form (55)–(58). The domain Ω is discretized into a finite number of elements, and each element is associated with a finite number of nodes. Then u and w are approximated by

$$u^h(\boldsymbol{x}, t) = \sum_{A \in \eta} d_A(t) N_A(\boldsymbol{x}), \tag{59}$$

$$w^h(\boldsymbol{x}) = \sum_{A \in \eta} w_A N_A(\boldsymbol{x}). \tag{60}$$

Here η is the set of nodes, N_A is the shape function associated with node A, and $d_A(t)$ and w_A are coefficients. We now substitute (59) and (60) into (55)–(58) with the sum over n truncated at some finite value N, and require the resulting equation to hold for all values of w_A. This yields the finite element matrix form of the problem for the vector of unknowns $\boldsymbol{z} = \boldsymbol{z}(t)$:

$$\begin{aligned}
\boldsymbol{M}\ddot{\boldsymbol{z}} + \boldsymbol{C}\dot{\boldsymbol{z}} + \boldsymbol{K}\boldsymbol{z} &= \boldsymbol{f}, \quad t > 0 && (61) \\
\dot{\boldsymbol{\psi}}_{nm}(t) &= \boldsymbol{A}_n \boldsymbol{\psi}_{nm}(t) + \left(u|_{r=1}, Y_{nm} \right) \boldsymbol{e}_n, \quad \boldsymbol{\psi}_{nm}(0) = 0 && (62) \\
\boldsymbol{z}(0) &= \boldsymbol{z}_0 && (63) \\
\dot{\boldsymbol{z}}(0) &= \boldsymbol{v}_0. && (64)
\end{aligned}$$

The matrices $\boldsymbol{M}$, $\boldsymbol{K}$, and $\boldsymbol{C}$, are defined by

$$\begin{aligned}
&\boldsymbol{M} = [M_{AB}], \;\; \boldsymbol{K} = [K_{AB}], \;\; \boldsymbol{C} = [C_{AB}], && (65) \\
&M_{AB} = (N_A, N_B), \;\; K_{AB} = (\nabla N_A, c\nabla N_B), \;\; C_{AB} = (N_A, N_B)_{\mathcal{B}}. && (66)
\end{aligned}$$

The vectors $\boldsymbol{f}$, $\boldsymbol{z}_0$, and $\boldsymbol{v}_0$ are defined by

$$\boldsymbol{f} = \{f_A\}, \;\; \boldsymbol{z}_0 = \{z_{B0}\}, \;\; \boldsymbol{v}_0 = \{v_{B0}\}, \tag{67}$$

$$f_A = (N_A, f) - \sum_{n=1}^{N} \sum_{m=-n}^{n} \boldsymbol{d}_n \cdot \boldsymbol{\psi}_{nm} \, (N_A, Y_{nm})_{\mathcal{B}}, \tag{68}$$

$$d_{B0} = (u_0, N_B), \;\; v_{B0} = (\dot{u}_0, N_B). \tag{69}$$

The quantities $\boldsymbol{z}$, $\dot{\boldsymbol{z}}$, and $\ddot{\boldsymbol{z}}$ are the displacement, the velocity, and the acceleration vectors, respectively. $\boldsymbol{M}$ is the mass matrix, $\boldsymbol{K}$ is the stiffness matrix, and $\boldsymbol{C}$ is a damping term due to the absorbing boundary condition. We note that $\boldsymbol{M}$ is symmetric and positive definite, and that both $\boldsymbol{K}$ and $\boldsymbol{C}$ are symmetric and positive semi-definite. Thus, we can use a standard time-marching scheme from the Newmark [16] family, such as the central difference method, to integrate (61). The solution to (62) is computed concurrently, for instance using the implicit trapezoidal rule (see Section 4.3). The matrix $\boldsymbol{C}$ is almost empty, since only terms along the boundary contribute to its nonzero entries. Further implementation details on the combination of the finite element method with the nonreflecting boundary condition can be found in [14].

4.3 Finite Difference Formulation

Instead of using the finite element method, we can use a finite difference method to solve (47)–(51). We shall now describe how to do this, choosing $c(\boldsymbol{x}) = 1$ in Ω for simplicity.

We opt for the leap-frog method, which is a standard *explicit* time-marching method for the wave equation. The wave equation (47) is discretized both in time and in space using second-order centered finite differences. We denote by U^h the numerical grid function. Let U^k be the numerical solution and f^k the source f at some grid point $\boldsymbol{x}$ at time $t_k = k\Delta t$. Then the basic step to advance the numerical solution in time is

$$U^{k+1} = 2U^k - U^{k-1} + (\Delta t)^2(\Delta^h U^k + f^k), \qquad k = 1, 2, \ldots \tag{70}$$

Here Δ^h denotes a finite difference approximation to the Laplacian.

The boundary condition (50) is necessary when we wish to advance the numerical solution on $\mathcal{B}$ using (70). Indeed, the radial part of Δ^h requires values of U^h outside Ω. Let $\Delta_r u = r^{-2}\partial_r(r^2\partial_r u)$ denote the radial part of the Laplacian. Next, let r_ℓ denote the ℓ-th grid point in the radial direction. Hence $r_{\ell+1} = r_\ell + \Delta r$, and $r_{\ell+1/2} = r_\ell + \Delta r/2$. Then a second-order finite difference approximation to Δ_r is

$$\Delta_r^h U_\ell = \frac{r_{\ell+1/2}^2\, U_{\ell+1} - (r_{\ell+1/2}^2 + r_{\ell-1/2}^2)\, U_\ell + r_{\ell-1/2}^2\, U_{\ell-1}}{(r_\ell \Delta r)^2}. \tag{71}$$

To calculate $\Delta_r^h U^h$ at $r_\ell = R$, we need $U_{\ell+1}$ which lies outside Ω. We eliminate it by using the finite difference approximation to (50) at $r_\ell = R$, θ_i, φ_j, with the sum over n truncated at some finite value N. This yields

$$\frac{r_{\ell+1}\,U^k_{\ell+1} - r_{\ell-1}\,U^k_{\ell-1}}{2\Delta r} + \frac{r_\ell\,(U^{k+1}_\ell - U^{k-1}_\ell)}{2\Delta t} = -\sum_{n=1}^{N}\sum_{m=-n}^{n} \boldsymbol{d}_n \cdot \boldsymbol{\psi}^k_{nm}\,Y_{nm}(\theta_i,\varphi_j). \tag{72}$$

Thus we have the two equations (70) and (72) for the two unknowns U^{k+1}_ℓ and $U^k_{\ell+1}$, which enables us to solve for U^{k+1}_ℓ on $\mathcal{B}$. We note that to compute U^{k+1} on $\mathcal{B}$, we only need the values of $\boldsymbol{\psi}_{nm}(t)$ at $t = t_k$, because both the differential equation and the boundary condition are discretized in time about $t = t_k$. The amount of memory needed to store the $\boldsymbol{\psi}_{nm}(t)$ with $n \leq N$, about $(2/3)N^3$ scalar values, is negligible when compared to the storage required for u inside Ω.

The numerical solution $\boldsymbol{\psi}^h_{nm}$ to the ordinary differential equation (46) is computed concurrently with U^h. Because the eigenvalues of $\boldsymbol{A}_n$ lie in the left half of the complex plane (see Figure 6), we opt for the implicit second-order trapezoidal rule ([17], p. 199):

$$\left(I - \frac{\Delta t}{2}\boldsymbol{A}_n\right)\boldsymbol{\psi}^{k+1}_{nm} = \left(I + \frac{\Delta t}{2}\boldsymbol{A}_n\right)\boldsymbol{\psi}^k_{nm} + \frac{\Delta t}{2}\left(U^{k+1} + U^k\Big|_{r=R}, Y_{nm}\right)\boldsymbol{e}_n. \tag{73}$$

The inner products $(Y_{nm}, U^h|_{r=R})$ are computed using Simpson's fourth order quadrature rule. Since the trapezoidal rule is unconditionally stable, there is no restriction on Δt for stability reasons, besides that imposed by the leap-frog method. The work required in solving the linear systems (73) is negligible, because the matrices $\boldsymbol{A}_n$ are very small and do not change with time.

The complete algorithm proceeds as follows:

ALGORITHM:

0. Initialize U^h at t_0 and t_1, and set $\boldsymbol{\psi}^0_{nm}$ and $\boldsymbol{\psi}^1_{nm}$ to zero.
1. Compute U^{k+1} at $t_{k+1} = t_k + \Delta t$ at all inner points of Ω using the difference form of (70).
2. Compute U^{k+1} at t_{k+1} and $r = R$ using (70) and (72).
3. Compute $\boldsymbol{\psi}^{k+1}_{nm}$ at t_{k+1} using (73), and return to 1.

Most of the work involved in applying the boundary condition results from computing the inner products over $\mathcal{B}$ on the right side of (73). To compute these inner products it is not necessary to compute $O(N^2)$ inner products over the entire sphere. Indeed, since the spherical harmonics $Y_{nm}(\theta, \phi)$ separate in θ and ϕ, it is sufficient to compute $O(N)$ inner products with $\cos(m\phi)$ and $\sin(m\phi)$ over the sphere, and then to compute $O(N^2)$ *one-dimensional* inner products in θ over $[0, \pi]$. The same method can be used to calculate the sums over n and m on the right of (72). In all our computations we have found $N \leq 25$ to be sufficient. If very large values of N were needed, the work and storage required could be reduced by an order of magnitude by combining the fast discrete polynomial transform of Driscoll, Healy, and Rockmore [18] with the recent work of Alpert, Greengard, and Hagstrom [19] on the approximation of boundary integral kernels – see also Hagstrom [20].

4.4 Modified boundary conditions

In computation, the sum over n in (45) must be truncated at a finite value N. Then the boundary condition becomes inexact for the modes beyond the point of truncation. It reduces to $(\partial_r + \partial_t)[ru_{nm}] = 0$ at $r = R$ for the modes $u_{nm} = (U, Y_{nm})$, $n > N$. This raises the question whether we can replace this inexact condition by a more accurate one, as we did in [21] for the reduced wave equation. We shall show how to modify the truncated boundary condition so that it remains exact for the low modes $n \leq N$, but becomes more accurate for the high modes $n > N$.

In deriving (36), we applied $B_1 = \partial_r + \partial_t$ to (34). This operator annihilates any spherically symmetric outgoing wave, such as the leading term of the large r expansion of $ru(\boldsymbol{x}, t)$, where u is any solution of (16):

$$ru(r, \theta, \phi, t) = \sum_{j=0}^{\infty} \frac{g_j(ct - r, \theta, \phi)}{r^j}, \quad r \geq a. \tag{74}$$

Bayliss and Turkel [22] derived a sequence of local operators, which annihilate increasingly many leading terms in (74). We shall now derive an equivalent sequence of operators B_ℓ, which look slightly different because we work with ru instead of u. Then we shall show how to use them to modify the boundary condition (46).

To derive these operators, we note that for any $m \geq 0$

$$\left(\frac{\partial}{\partial r} + \frac{1}{c}\frac{\partial}{\partial t} + \frac{m}{r} \right) \frac{g(ct - r)}{r^m} = 0. \tag{75}$$

We use (74) and (75) with $m = 2$ to obtain

$$B_2[ru] = \left(\frac{\partial}{\partial r} + \frac{1}{c}\frac{\partial}{\partial t} + \frac{2}{r}\right)\left(\frac{\partial}{\partial r} + \frac{1}{c}\frac{\partial}{\partial t}\right)[ru] = \sum_{j=2}^{\infty} \frac{j(j-1)\, g_j}{r^{j+2}}. \tag{76}$$

Next we use (74) and (75) with $m = 3$ to get

$$\begin{aligned} B_3[ru] &= \left(\frac{\partial}{\partial r} + \frac{1}{c}\frac{\partial}{\partial t} + \frac{4}{r}\right)\left(\frac{\partial}{\partial r} + \frac{1}{c}\frac{\partial}{\partial t} + \frac{2}{r}\right)\left(\frac{\partial}{\partial r} + \frac{1}{c}\frac{\partial}{\partial t}\right)[ru] \\ &= \sum_{j=3}^{\infty} \frac{-j(j-1)(j-2)\, g_j}{r^{j+3}}. \end{aligned} \tag{77}$$

For $\ell \geq 1$, we define the operator B_ℓ

$$B_\ell = \prod_{j=0}^{\ell-1} \left(\frac{\partial}{\partial r} + \frac{1}{c}\frac{\partial}{\partial t} + \frac{2j}{r}\right), \tag{78}$$

where the rightmost term is $j = 0$. Upon applying B_ℓ to (74), we find that

$$B_\ell[ru] = \mathcal{O}\left(r^{-2\ell}\right), \quad r \geq R. \tag{79}$$

Instead of applying $B_1 = \partial_r + \partial_t$ to (34), we can apply a higher order differential operator B_ℓ with $\ell > 1$. Thus, when the sum over n is truncated at a finite value N, the boundary condition on the modes $n > N$ becomes

$$B_\ell[ru] = 0, \qquad r = R. \tag{80}$$

In view of (79), we expect that using (80) with $\ell > 1$ instead of with $\ell = 1$ will yield a smaller error.

When we apply B_2 to (34) and use (33), we get

$$B_2[ru_{nm}(r,t)] = \sum_{j=2}^{n} \frac{j(j-1)\ \gamma_{nj}}{r^{j+2}\, c^{n-j}} \frac{\partial^{n-j}}{\partial t^{n-j}} G_n[u_{nm}](r,t), \quad r \geq R. \tag{81}$$

Similarly, when we apply B_3 to (34) we get

$$B_3[ru_{nm}(r,t)] = -\sum_{j=3}^{n} \frac{j(j-1)(j-2)\ \gamma_{nj}}{r^{j+3}\, c^{n-j}} \frac{\partial^{n-j}}{\partial t^{n-j}} G_n[u_{nm}](r,t), \quad r \geq R. \tag{82}$$

We note that the term $j = 1$ in (36) vanishes in (81), and that the terms $j = 1$ and $j = 2$ vanish in (82). As a consequence, $B_2[ru] = 0$ is an exact boundary condition for the modes $n = 0, 1$, and $B_3[ru] = 0$ is an exact boundary condition for the modes $n = 0, 1, 2$. Hence, annihilating the leading ℓ terms of the large distance expansion (74) naturally imposes the exact boundary condition on the modes $0 \leq n \leq \ell - 1$.

For later reference, we derive the full boundary condition with $\ell = 2$. We multiply (81) by Y_{nm}, and sum over n and m. Next, we set $r = R$, and use (38) to obtain

$$B_2[ru] = \sum_{n=2}^{\infty} \sum_{m=-n}^{n} \tilde{\boldsymbol{d}}_n \cdot \boldsymbol{\psi}_{nm}(t) Y_{nm}, \quad r = R. \tag{83}$$

Here $\boldsymbol{\psi}_{nm}(t)$ is the solution of (46), and $\tilde{\boldsymbol{d}}_n$ replaces $\boldsymbol{d}_n$ in (45):

$$\tilde{\boldsymbol{d}}_n(j) = \frac{j(j-1)\, n(n+1)}{2}, \; j = 1, \ldots, n. \tag{84}$$

5 Numerical Examples

We shall now compare the accuracy of various boundary conditions via two numerical experiments. First, we shall present a detailed study of the accuracy and the convergence properties of different boundary conditions. To do so, we shall consider a model problem, where a locally supported time-harmonic source excites the medium inside Ω. Here we shall also demonstrate the long-time stability of our numerical method. Second, we shall present computations for a standard test problem: radiation from a piston on a sphere.

5.1 Model problem

We consider the problem (47)–(51) with $c(\boldsymbol{x}) = 1$, and both u_0 and $\dot{u}_0$ equal to zero. In addition, we set a spherical obstacle Γ of radius 0.5 inside Ω. As the artificial boundary $\mathcal{B}$ is located at $R = 1$, the computational domain Ω is the region $0.5 \leq r \leq 1$. Initially, the medium is at rest; it is then excited locally by a time-harmonic source distributed within a sphere of radius $r_f = 0.15$ centered at $\boldsymbol{x}_f$ ($r = 0.75$ and $\theta = 0$). The source strength

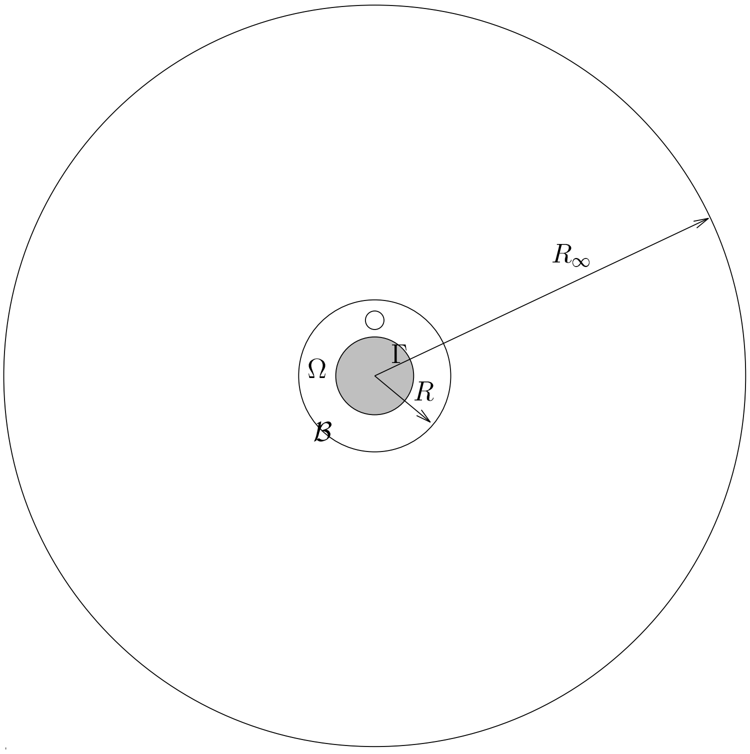

Figure 7: The computational domains Ω for U^h, and $0.5 \leq r \leq 5$ for U^h_∞, are shown drawn to scale. The support of f lies in the small sphere inside Ω, located above the obstacle (shaded area).

is

$$f(\boldsymbol{x}, t) = \begin{cases} \alpha \sin(\omega t) \sin^2((1 - |\boldsymbol{x} - \boldsymbol{x}_f|/r_f)\pi/2) & \text{if } |\boldsymbol{x} - \boldsymbol{x}_f| < r_f, \\ 0 & \text{otherwise.} \end{cases} \tag{85}$$

We choose the scaling constant $\alpha = 5 \times 10^4$ to make the solution $\mathcal{O}(1)$. The source f has its maximal value at $\boldsymbol{x}_f$, and decays with distance from $\boldsymbol{x}_f$.

We shall compare the numerical solution U^h of (47)–(51) with the numerical solution U^h_∞ of (47)–(49) in the infinite domain. To compute U^h_∞ we consider the larger domain $|\boldsymbol{x}| \leq R_\infty$, with $R_\infty = 5$. Since the propagation speed c is one, and since the support of f lies inside Ω, the influence of the boundary at $r = R_\infty$ will not be sensed inside Ω until $t = 8$. Therefore inside Ω, U^h_∞ coincides with the numerical solution of the initial-boundary value problem in the infinite region outside the obstacle Γ for $0 \le t \le 8$. The setup for this model problem is drawn to scale in Figure 7.

The instantaneous error $E^h(t)$ is defined as

$$E^h(t) = \|U^h_\infty(.,t) - U^h(.,t)\|_{L_2(\Omega)}. \tag{86}$$

We denote by E^h_T the maximal error over the time interval $[0, 8]$,

$$E^h_T = \max_{t\in[0,8]} E^h(t). \tag{87}$$

Since the amplitude of the solution is determined by f, which can be scaled by any constant, the magnitude of the absolute error $E^h(t)$ is irrelevant. We shall only use it as a means to compare the performance of the various boundary conditions in relationship to one another.

5.1.1 Implementation details

The test problem described above is axisymmetric and independent of φ. Therefore, it suffices to compute the solution in the r, θ plane for $0 \le \theta \le \pi$, with the symmetry condition $\partial_\theta u = 0$ at $\theta = 0$ and $\theta = \pi$. The grid in Ω is evenly spaced with 10, 20, or 40 intervals in $0.5 \le r \le 1$, and 60, 120, or 240 intervals in $0 \le \theta \le \pi$, respectively. For the computation of U^h_∞, we simply extend the mesh into the larger domain with the same grid spacing up to $r = R_\infty$. Both U^h and U^h_∞ are computed using the explicit second-order leap-frog method described in Section 4.3 .

The stability condition for the leap-frog method on an equispaced grid with spacing h, in three space dimensions, and with $c = 1$, is $\Delta t \le h/\sqrt{3}$. Since we shall use a polar grid, we simply set Δt equal to the shortest edge in the mesh divided by $\sqrt{3}$. We keep Δt fixed throughout the computation. In Figure 8, the solution U^h_∞ is shown at $t = 3.5$ for a frequency $\omega = 2\pi$, just before the wave front reaches the external boundary $r = R_\infty$.

We shall compute U^h by using various boundary conditions at $\mathcal{B}$. The boundary condition (80) with $\ell = 1$ and $\ell = 2$ is denoted by BT1 and BT2, respectively, to acknowledge [22]. We denote (45) by NR1(N) and (83) by NR2(N). We recall that NR1(0) coincides with BT1, and that NR2(0) and NR2(1) coincide with BT2.

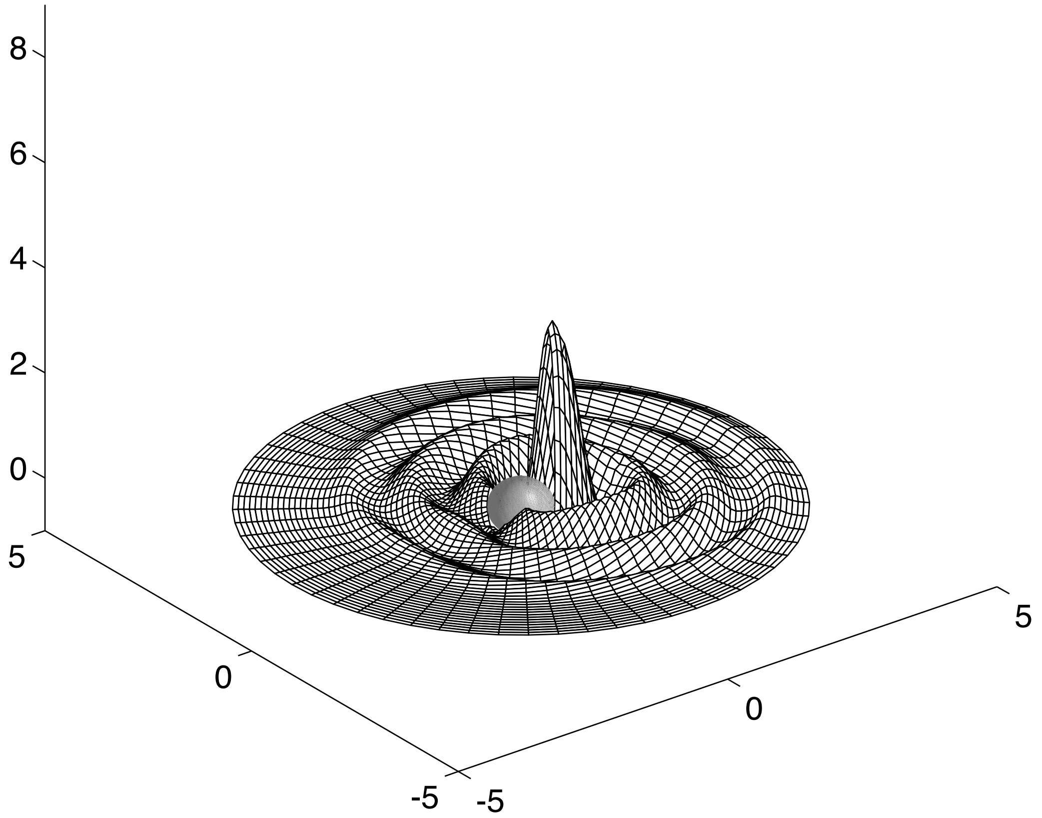

Figure 8: The solution U^h_∞ at $t = 3.5$ is shown for $\omega = 2\pi$.

To implement (83), we first expand B_2 as

$$B_2 = \frac{\partial^2}{\partial r^2} + \frac{\partial^2}{\partial t^2} + 2\frac{\partial^2}{\partial r \partial t} + \frac{2}{r}\left(\frac{\partial}{\partial r} + \frac{\partial}{\partial t}\right). \tag{88}$$

All the terms but the cross derivatives can be approximated with a second-order finite difference formula centered at $r = R$ and $t = t_k$. The radial derivative in the term $\partial_r \partial_t$ is approximated by second-order extrapolation into Ω, by passing a parabola through rU^h at the grid locations $r_{\ell-2}$, $r_{\ell-1}$, and $r_\ell = R$.

5.1.2 Numerical results

We begin with a calculation at the low frequency $\omega = \pi/4$ on the 20×120 grid. In Figure 9 we compare the solutions obtained using BT1, BT2, and NR1(20), with the "exact" solution U^h_∞. The solution is shown at the north pole of $\mathcal{B}$, $r = 1$ and $\theta = 0$, as a function of time. Both BT1 and BT2 yield rather large errors. The solution obtained using NR1(20) cannot be distinguished from U^h_∞ on the left graph. The error $E^h(t)$ is shown on the

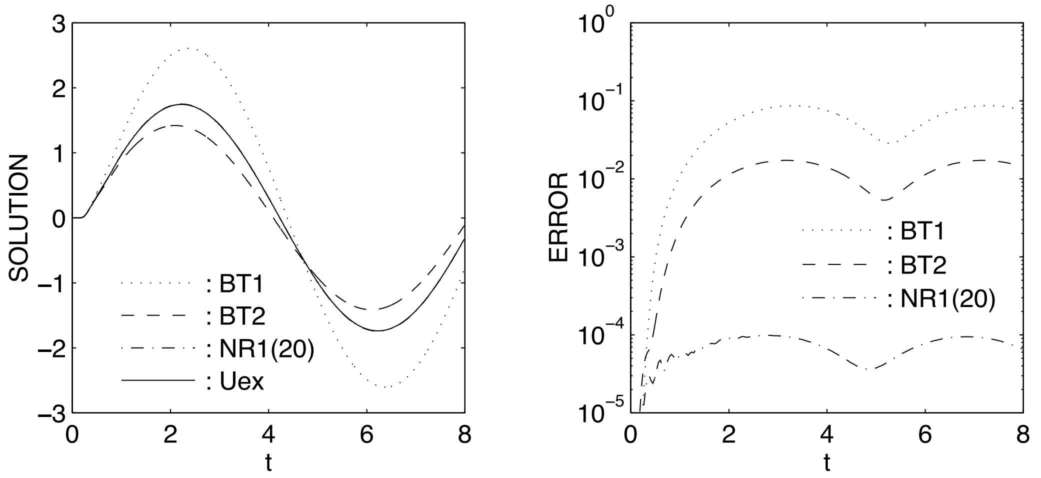

Figure 9: Results for $\omega = \pi/4$. Left: The solutions U^h, computed using the boundary conditions BT1, BT2, and NR1(20), are compared with the exact solution U^h_∞ on $\mathcal{B}$ at $\theta = 0$. Right: The L_2 error $E^h(t)$ is shown for the same three boundary conditions.

right. By using NR1(20) instead of BT1 or BT2, the error is reduced by almost three orders of magnitude in accuracy. The error in using NR1(20) is mainly due to the discretization error, and not to the boundary condition.

We shall now verify that the numerical solution U^h computed using NR1(N) indeed converges to U^h_∞ inside Ω if N is large enough. We set $N = 25$, and progressively refine the initial grid 10×60 by a factor two in r and in θ. At each refinement, the error drops by a factor four, as is shown in Figure 10. This shows the second-order convergence to the exact solution U^h_∞ as $\Delta r, \Delta t \to 0$. In that sense the boundary condition is exact, even if truncated and used in a numerical scheme: the error introduced at the boundary is negligible in comparison to the discretization error of the numerical method used in the interior of Ω. In contrast, the solutions obtained using BT1 and BT2 do not improve as we refine the mesh. This clearly indicates that the error introduced by imposing them at $\mathcal{B}$ dominates in the computation. If one refines the mesh further, it may be necessary to increase the value of N to ensure that the error due to the boundary condition remains negligible.

Next, we compare the solutions U^h computed with the boundary condi-

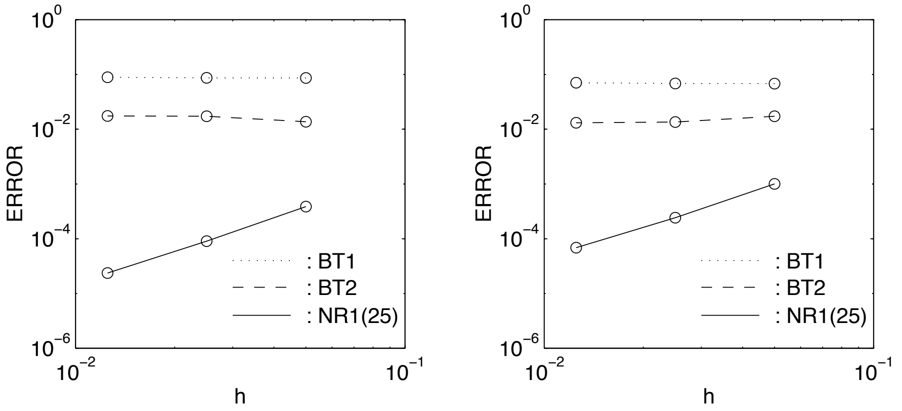

Figure 10: The maximal errors E_T^h in the numerical solutions U^h, computed with the boundary condition NR1(25) on the three grids 10×60, 20×120, and 40×240, are shown versus $h = \Delta r$. Left: for $\omega = \pi/4$. Right: for $\omega = \pi$.

tions NR1(N) and NR2(N). The grid 20×120 is kept fixed while we increase the value of N. We recall that NR1(0) is identical to BT1, and that NR2(0) and NR2(1) are identical to BT2. Figure 11 shows that we obtain an improvement of two or three orders in magnitude over BT1 and BT2 if we use the exact boundary condition. We attribute the small discrepancy between NR1 and NR2 for large values of N to the less accurate finite difference approximation used in (88).

Figure 11 also displays the subtle interplay between the error due to discretization, and the error due to truncating the boundary condition. For a fixed grid, there is a maximal value for N, below which the error does not decrease anymore. From that point on, the boundary condition becomes more accurate than the numerical method, and it is pointless to increase N without further refining the underlying mesh.

5.1.3 Long time stability

The issue of long time stability has arisen in the numerical implementation of the exact boundary condition due to Ting and Miksis [6] – see also Section 4.

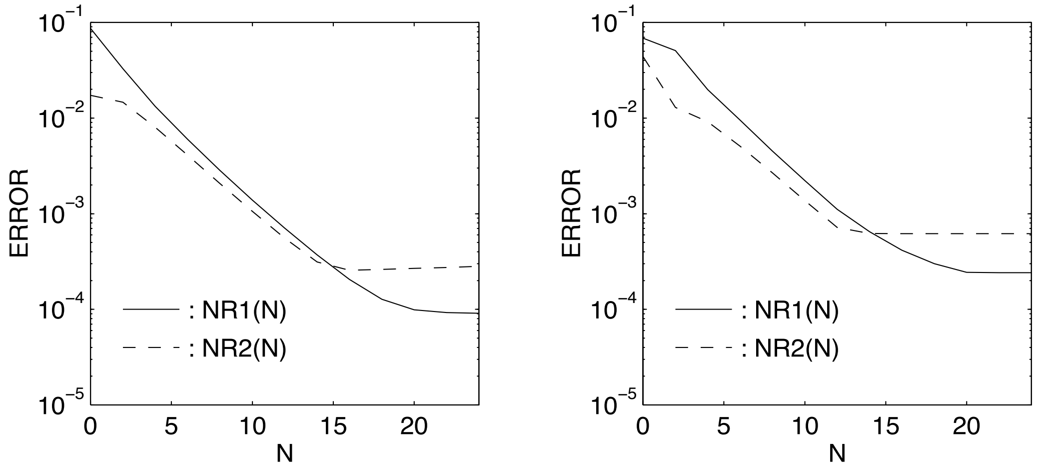

Figure 11: The maximal errors E_T^h in the numerical solutions, computed on the grid 20×120 using the boundary conditions NR1(N) and NR2(N), are shown versus N. Left: for $\omega = \pi/4$. Right: for $\omega = \pi$.

By using Kirchhoff's formula for the time-dependent wave equation in three space dimensions, they derived an exact nonreflecting boundary condition. It is nonlocal in both space and time, but involves only a fixed amount of past information. When Givoli and Cohen [7] combined this boundary condition with a standard nondissipative finite-difference scheme in the interior domain, the numerical solution exhibited a long time instability. They were able to eliminate this instability by using the dissipative Lax-Wendroff scheme in the interior domain. In contrast, the boundary conditions, which were derived in Section 4 and combined with a nondissipative second-order centered finite difference stencil inside Ω, never exhibited any unstable behavior. Whether the explicit Adams method or the trapezoidal rule was used to integrate the system of ordinary differential equations on the artificial boundary, the overall numerical scheme was stable in all our test runs.

To demonstrate the long time stability of our numerical method, we proceed as in [7]. We consider the model problem with the source f a short-time pulse, that is with the temporal part $\sin(\omega t)$ of $f(\boldsymbol{x}, t)$ set to zero for $t \geq \pi/\omega$. In Figure 12, the solutions U^h for $\omega = \pi/4$, using the boundary conditions BT1, BT2, NR1(20), and NR2(20), are shown on $\mathcal{B}$ at $\theta = 0$ for a long time

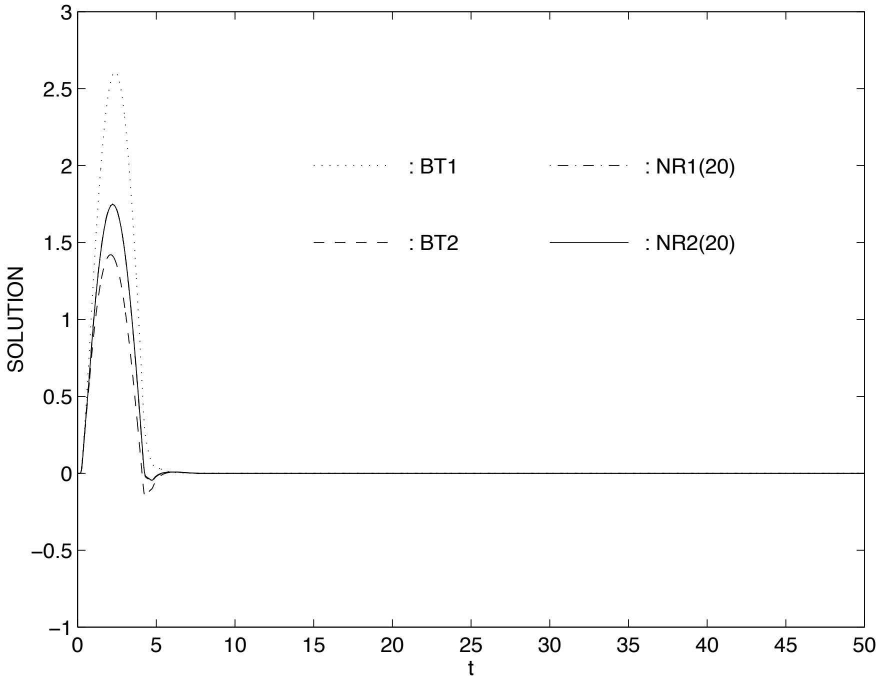

Figure 12: Demonstration of long time stability: the solutions U^h, computed with $f(\boldsymbol{x}, t)$ a short-time pulse using the boundary conditions BT1, BT2, NR1(20), and NR2(20), are shown on $\mathcal{B}$ at $\theta = 0$.

interval. The results indicate that the numerical method using any one of these boundary conditions is stable.

5.2 Piston on a sphere

Here we consider the radiation from a circular piston on a sphere of radius 0.5. The portion of the sphere from $\theta = 0°$ to $\theta = 15°$ is a piston, moving with radial velocity $\sin \omega t$. Elsewhere, the sphere is rigid and the solution vanishes. To avoid the extra numerical complications due to a discontinuous boundary condition, we let the solution decay smoothly to zero for $15° \leq \theta \leq 30°$. This problem is challenging because the waves generated at the piston pole $\theta = 0°$ are attenuated by a geometric spreading loss, as they travel along longitudes down to the south pole. In the region opposite the piston, the amplitude of the waves is significantly lower than it is near the piston.

Because this problem is symmetric about the z-axis, the acoustic field is

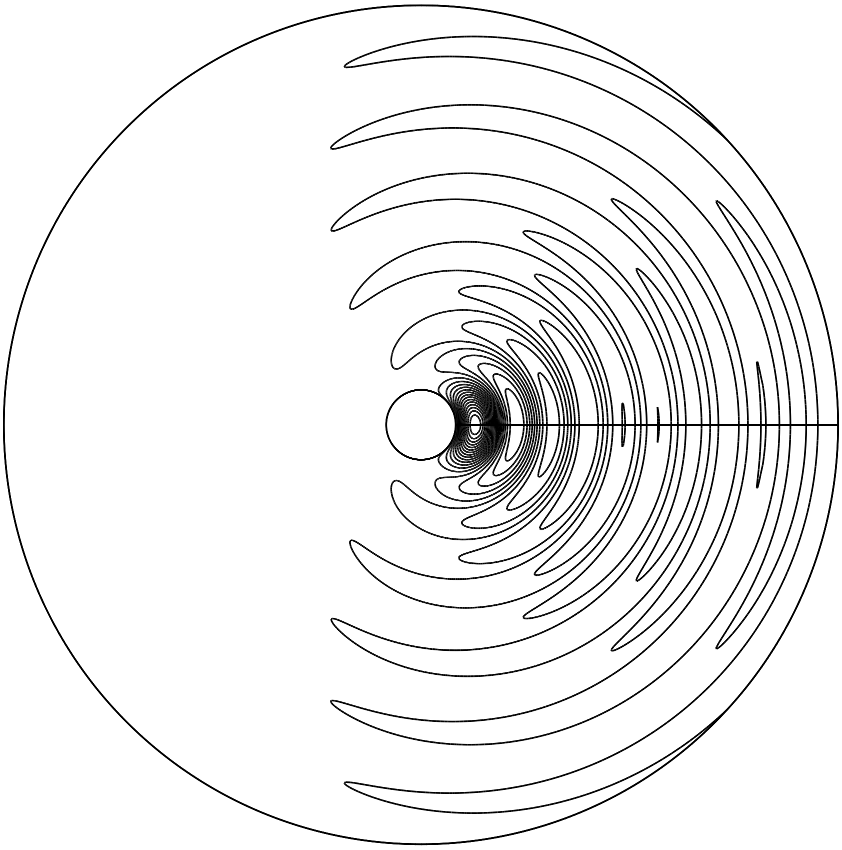

Figure 13: Piston on a sphere: the exact solution U^h_∞ is shown at $t = 10$ inside the large domain, $0.5 \leq r \leq 6$, with $\omega = 2\pi$.

independent of ϕ. Hence the computational domain Ω can be restricted to the two-dimensional region $r_0 \leq r \leq R$, $0 \leq \theta \leq \pi$, and the computational effort thus greatly reduced. Again we have truncated the unbounded exterior by a spherical artificial boundary at $r = R$. We choose $R = 1$ and use the finest mesh 40×240 inside Ω. For the "exact" solution U^h_∞, shown in Figure 13, we take the outer boundary at $R_\infty = 6$. Thus, the truncation at $r = R_\infty$ will not be sensed inside Ω until $t = 10.5$. In Figure 14, the contour lines for U^h_∞ and U^h are shown at time $t = 10$, where U^h is computed using BT2. We observe that U^h captures the physics of the solution quite well, especially in the vicinity of the piston. However, behind the sphere a spurious reflection

Figure 14: Piston on a sphere: the exact solution U^h_∞ (——) is compared with the solution U^h $(\cdot\cdot\cdot\cdot)$, computed inside Ω with the absorbing boundary condition BT2 applied at the artificial boundary.

from $\mathcal{B}$ travels towards the obstacle. The contour lines of U^h, calculated using NR1(20), coincide with those of U^h_∞ and cannot be discerned on this figure.

Since the spurious reflections introduced by the local boundary operators appear to be most severe at the south pole, we take a closer look at that region. On the left of Figure 15, the solutions U^h and U^h_∞ are shown at the south pole of $\mathcal{B}$, $r = 1$ and $\theta = 180°$, as functions of time. The solutions U^h are computed using BT1, BT2, and NR1(20). On the right of Figure 11, the same solutions are displayed at time $t = 10$ along the z-axis, $0.5 \leq r \leq 1$ and $\theta = 180°$. The solutions U^h_∞ and U^h, calculated using NR1(20) coincide almost perfectly. The solutions U^h, calculated using BT1 and BT2, differ significantly from the exact solution. The spurious reflections they introduce at the outer boundary, travel back into Ω and spoil the solution right up to the obstacle.

6 Conclusion

First, we wish to emphasize that this article makes no pretense of providing a complete presentation, not even a survey, of the rapidly growing literature in absorbing boundary conditions – see Givoli [1, 23] or more recently Tsynkov [24] for a review. In particular, we have completely ignored the popular approach of absorbing layers [25], which made a comeback in the mid-nineties with the perfectly matched layer (PML) method of Bérenger [26].

The constant demand for increasingly accurate, efficient, and robust nu-

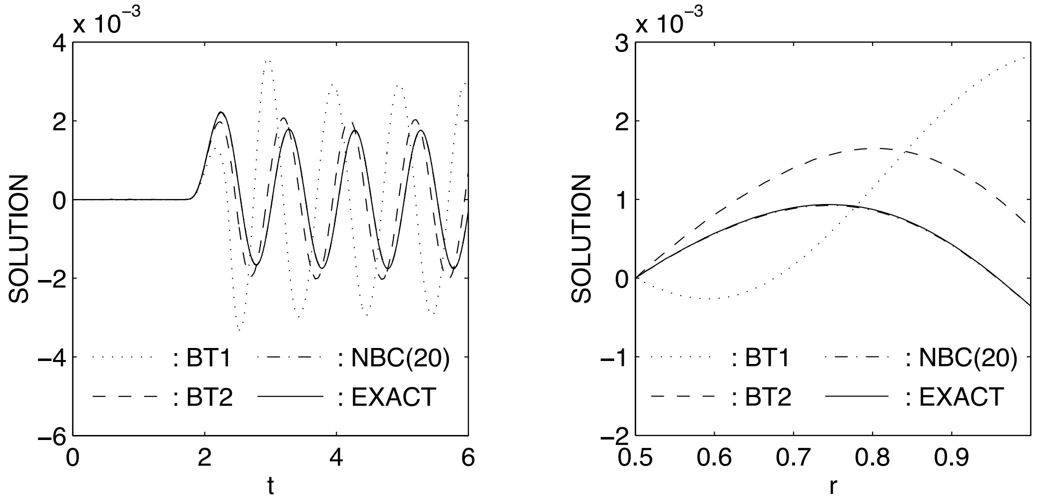

Figure 15: Piston on a sphere. Left: The solutions U^h, computed using the boundary conditions BT1, BT2, and NBC(20), are compared with the exact solution U^h_∞ on $\mathcal{B}$ at $\theta = \pi$. Right: The same four solutions are shown at $t = 10$ along the z-axis in the region below the south pole, at $\theta = \pi$ and $0.5 \leq r \leq 1$.

merical methods, which can handle a wide variety of physical phenomena, spurs the search for improvements in absorbing boundary conditions. The frustration is all too obvious, when the gains made in the interior by using sophisticated numerical methods, such as high order and adaptive methods, are annihilitated at the artificial boundary by the use of an inaccurate boundary condition. The exact nonreflecting boundary condition (45)–(46) has been found to be very accurate in numerical computations. It involves only first-order derivatives of the displacement, which makes it robust and easy to use. The boundary condition fits easily into finite-difference methods and allows the artificial boundary to be brought as close as desired to the scatterer. It is easy to implement and requires little extra storage and computer time. It also fits naturally into the variational formulation; hence it is well-suited for use with the finite element method. Although the formulation is global over the artificial boundary, it is explicit and does not require the solution of any large linear system. It only requires inner products with spherical harmonics of the displacement on the artificial boundary. Although the artificial boundary must be spherical, the boundary condition is not tied to any coordinate system, and the grid used inside Ω can be arbitrary. With the nonreflecting boundary condition the overall numerical scheme retains its optimal rate of convergence, as the error introduced at the artificial boundary can always be reduced below the discretization error due to the numerical method in the interior computational domain. Therefore the numerical scheme converges at little extra cost to the true solution in the unbounded region.

Acknowledgement

I would like to thank Joseph B. Keller for helpful comments and suggestions, and for reading the manuscript.

References

[1] D. Givoli, “Non-reflecting boundary conditions”, *J. Comp. Phys.* **94** 1, (1991).

[2] W. D. Smith, “Nonreflecting plane boundary for wave propagation problems”, *J. Comput. Phys.* **15**, 492 (1974).

[3] M. J. Grote and J. B. Keller, “Exact nonreflecting boundary conditions for the time dependent wave equation”, *SIAM J. Appl. Math.* **55**, 280 (1995).

[4] B. Engquist and A. Majda, “Absorbing boundary conditions for the numerical simulation of waves”, *Math. Comp.* **31**, 629 (1977).

[5] R. L. Higdon, “Numerical absorbing boundary conditions for the wave equation”, *Math. Comp.* **49**, 65 (1987).

[6] L. Ting and M. J. Miksis, “Exact boundary conditions for scattering problems”, *J. Acoust. Soc. Amer.* **80**, 1825 (1986).

[7] D. Givoli and D. Cohen, “Nonreflecting boundary conditions based on Kirchhoff-type formulae”, *J. Comput. Phys.* **117**, 102 (1995).

[8] M. J. Grote and J. B. Keller, “Nonreflecting boundary conditions for time dependent scattering”, *J. Comp. Phys.* **127**, 52 (1996).

[9] I. L. Sofronov, “Conditions for complete transparency on the sphere for the three-dimensional wave equation”, *Russian Acad. Sci. Dokl. Math.* **46**, 397 (1993).

[10] I. L. Sofronov, “Artificial boundary conditions of absolute transparency for two- and three-dimensional external time-dependent scattering problems”, *Europ. J. Appl. Math.* **9**, 561 (1998).

[11] M. J. Grote and J. B. Keller, “Nonreflecting boundary conditions for Maxwell’s equations”, *J. Comp. Phys.* **139**, 327 (1998).

[12] M. J. Grote and J. B. Keller, “Nonreflecting boundary conditions for elastic waves”, *SIAM J. Appl. Math.* **60**, 803 (2000).

[13] M. J. Grote, “Nonreflecting boundary conditions for elastodynamic scattering”, *J. Comput. Phys.*, in press.

[14] L. L. Thompson and R. Huan, “Implementation of exact non-reflecting boundary conditions in the finite element method for the time-dependent wave equation”, *Comput. Meth. Appl. Mech. Engin.*, in press.

[15] T. J. R. Hughes, *The Finite Element Method*, Prentice-Hall, 1987.

[16] N. M. Newmark, “A method of computation for structural dynamics”, *J. of Eng. Mech. Division*, ASCE, 67 (1959).

[17] E. Hairer, S. P. Nørsett, G. Wanner, *Solving Ordinary differential Equations I*, Springer Verlag, 1987.

[18] J. R. Driscoll, D. M. Healy, Jr., and D. N. Rockmore, “Fast discrete polynomial transforms with applications to data analysis for distance transitive graphs”, *SIAM J. Comput.* **26**, 1066 (1997).

[19] B. Alpert, L. Greengard and T. Hagstrom, “Rapid evaluation of nonreflecting boundary kernels for time-domain wave propagation”, *SIAM J. Numer. Anal.*, in press.

[20] T. Hagstrom, “Radiation boundary conditions for the numerical simulation of waves”, *Acta Numerica* (Cambridge University Press, 1999), p. 47.

[21] M. J. Grote and J. B. Keller, “On nonreflecting boundary conditions”, *J. of Comp. Phys.* **122**, 231 (1995).

[22] A. Bayliss und E. Turkel, “Radiation boundary conditions for wave-like equations”, *Comm. Pure Appl. Math.* **33**, 707 (1980).

[23] D. Givoli, *Numerical Methods for Problems in Infinite Domains* (Studies in Applied Mechanics 33, Elsevier, 1992).

[24] S. V. Tsynkov, “Numerical solution of problems on unbounded domains. A review”, *Appl. Num. Math.* **27**, 465 (1998).

[25] M. Israeli and S. A. Orszag, “Approximation of radiation boundary conditions”, *J. Comp. Phys.* **41**, 115 (1981).

[26] J.-P. Bérenger, “A perfectly matched layer for the absorbtion of electromagnetic waves”, *J. Comp. Phys.* **114**, 185 (1994).

Research Reports

No.	Authors	Title
00-04	M.J. Grote	Nonreflecting Boundary Conditions for Time Dependent Wave Propagation
00-03	M.H. Gutknecht	On Lanczos-type methods for Wilson fermions
00-02	R. Sperb, R. Strebel	An alternative to Ewald sums. Part 3: Implementation and results
00-01	T. Werder, K. Gerdes, D. Schötzau, C. Schwab	*hp* Discontinuous Galerkin Time Stepping for Parabolic Problems
99-26	J. Waldvogel	Jost Bürgi and the Discovery of the Logarithms
99-25	H. Brunner, Q. Hu, Q. Lin	Geometric meshes in collocation methods for Volterra integral equations with proportional time delays
99-24	D. Schötzau, Schwab	An *hp* a-priori error analysis of the DG time-stepping method for initial value problems
99-23	R. Sperb	Optimal sub- or supersolutions in reaction-diffusion problems
99-22	M.H. Gutknecht, M. Rozložník	Residual smoothing techniques: do they improve the limiting accuracy of iterative solvers?
99-21	M.H. Gutknecht, Z. Strakoš	Accuracy of Two Three-term and Three Two-term Recurrences for Krylov Space Solvers
99-20	M.H. Gutknecht, K.J. Ressel	Look-Ahead Procedures for Lanczos-Type Product Methods Based on Three-Term Lanczos Recurrences
99-19	M. Grote	Nonreflecting Boundary Conditions For Elastodynamic Scattering
99-18	J. Pitkäranta, A.-M. Matache, C. Schwab	Fourier mode analysis of layers in shallow shell deformations
99-17	K. Gerdes, J.M. Melenk, D. Schötzau, C. Schwab	The *hp*-Version of the Streamline Diffusion Finite Element Method in Two Space Dimensions
99-16	R. Klees, M. van Gelderen, C. Lage, C. Schwab	Fast numerical solution of the linearized Molodensky problem
99-15	J.M. Melenk, K. Gerdes, C. Schwab	Fully Discrete *hp*-Finite Elements: Fast Quadrature
99-14	E. Süli, P. Houston, C. Schwab	*hp*-Finite Element Methods for Hyperbolic Problems
99-13	E. Süli, C. Schwab, P. Houston	*hp*-DGFEM for Partial Differential Equations with Nonnegative Characteristic Form
99-12	K. Nipp	Numerical integration of differential algebraic systems and invariant manifolds